nature microbiology

Article

https://doi.org/10.1038/s41564-025-02168-4

Structural and mechanistic insights into herpesvirus helicase–primase and its therapeutic inhibitors

Received: 27 January 2025

Accepted: 30 September 2025

Published online: 4 November 2025

Check for updates

Qing Yao ✉, Alexandre Mercier ✉, Arabinda Nayak, Lindsey May, Pui Yan Ho, Ariel Lewis-Ballester, Varsha Nair, Annapurna Sapre, Thomas Aeschbacher, Jit Mukherjee, Christopher Richards, Roberto Mateo, Aesop Cho, Eric Lansdon & Xinchao Yu

The herpes simplex virus (HSV) helicase–primase (HP) complex is a promising anti-herpes therapeutic target. However, progress in developing highly effective small-molecule HP inhibitors (HPIs) for the treatment of genital herpes has been hindered by the lack of structural information on the HP complex and the incomplete understanding of the mechanism of action of HPIs. Here we present the cryogenic electron microscopy structure of the HSV-1 HP apo-complex (3.8 Å), along with structures bound to pritelivir (3.2 Å) and amenamevir (3.2 Å)—two clinically active, chemically distinct HPIs. The potency of both inhibitors against HSV variants bearing mutations within the HPI binding pocket supports the high-resolution mapping of key molecular interactions while revealing residues that govern their antiviral spectrum against alphaherpesviruses. Our results provide important insight into the unique architecture of the HP complex and the mechanism of inhibition of HPIs, paving the way for the development of next-generation antivirals to treat herpesvirus infections.

Billions of people are infected with at least one human herpesvirus[1]. While these lifelong infections are typically asymptomatic for extended periods of time owing to viral latency, lytic reactivation can occur spontaneously, which often leads to clinical manifestations. For example, reactivation of herpes simplex virus (HSV) type 1 (HSV-1) and type 2 (HSV-2) is associated with the development of both oral and genital herpes, while that of varicella zoster virus (VZV) causes herpes zoster (also known as shingles). These α-herpesvirus infections are also a major disease burden in immunocompromised hosts, causing a wide spectrum of life-threatening sequelae (for example, encephalitis and pneumonitis)[2,3], while a growing body of evidence points towards an association between these pathogens and an increased risk of dementia in older adults, including Alzheimer's disease[4–7]. Standard-of-care therapies for HSV and VZV infections are typically nucleoside analogues that target the viral DNA polymerase (for example, acyclovir, valacyclovir and famciclovir). These therapies have favourable safety profiles, but their inability to completely abrogate genital herpes recurrences and transmission[8,9] and the emergence of resistance in immunocompromised patients have highlighted the need for alternative therapeutic approaches[10].

The HSV helicase–primase (HP) complex includes three components: a helicase (UL5), a primase (UL52) and a non-catalytic subunit (UL8) that resembles a DNA polymerase. Sequence analysis revealed that UL5 contains seven key motifs characteristic of superfamily 1 (SF1) helicases, similar to those found in cellular helicases such as Pif1[11], RecB[12] and RecD2[13]. UL52 has an archaeo-eukaryotic primase (AEP) domain, which harbours the primase catalytic core, and a C-terminal zinc-finger motif. UL8, while not enzymatically active, probably has a DNA polymerase-like fold (Extended Data Fig. 1a). The HP complex acts at the viral replication fork, upstream of the viral DNA polymerase, by unwinding double-stranded DNA and depositing RNA primers on the lagging strand[14]. Given its critical role in viral DNA replication and

Gilead Sciences Inc., Foster City, CA, USA. ✉e-mail: qing.yao1@gilead.com; alexandre.mercier@gilead.com

https://doi.org/10.1038/s41564-025-02168-4

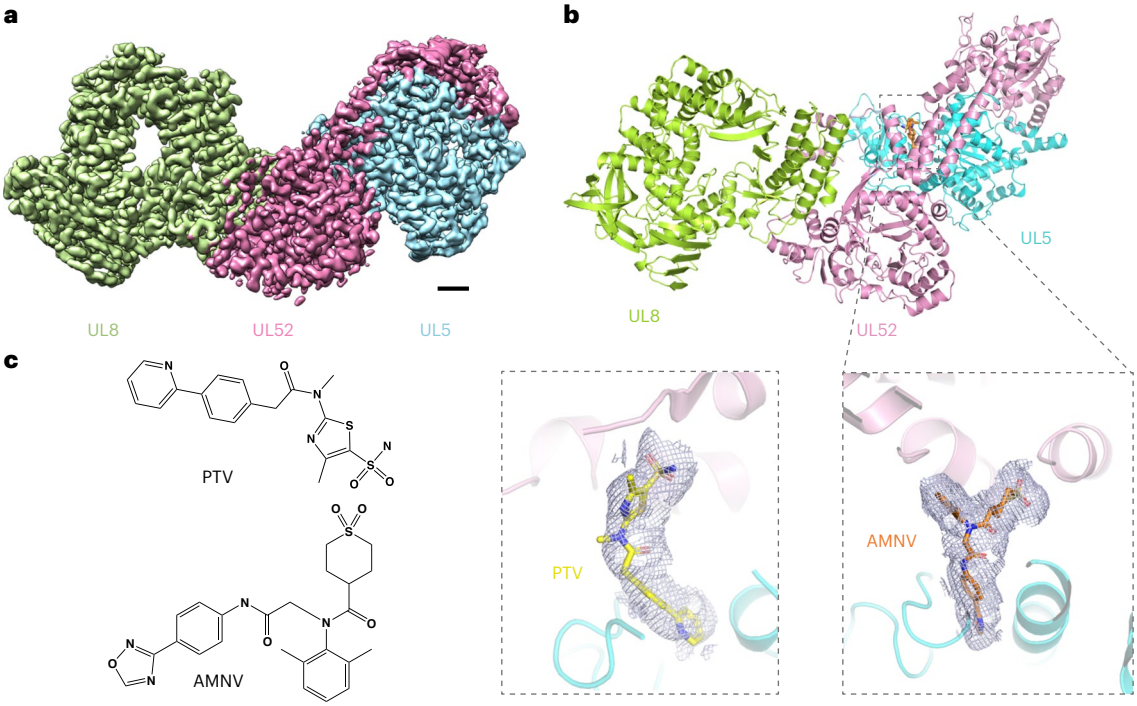

Fig. 1 | Architecture of the HSV-1 HP complex bound to PTV and AMNV. **a**, Overview of the HSV-1 HP complex with the AMNV composite map, created by combining separately refined maps of two bodies. The surface volume is colour-coded as indicated below. Scale bar, 10 Å. **b**, Ribbon diagram of the solved HSV-1 HP complex structure with AMNV. In the lower right image, AMNV is shown as a stick model with experimental density contoured at 1.0σ, while in the lower left image, PTV is presented as a stick model with experimental density also contoured at 1.0σ. The colour scheme is consistent across all figures unless otherwise noted. **c**, Chemical structures of PTV and AMNV.

the absence of an equivalent enzymatic complex in host cells, the HP complex has emerged as a promising antiviral target[15]. The small molecule HP inhibitor (HPI) pritelivir (PTV) is in phase III clinical trials for the treatment of acyclovir-resistant mucocutaneous HSV infections in immunocompromised patients[16]. Another HPI, amenamevir (AMNV), is approved in Japan for the treatment of both shingles and genital herpes[17,18]. While in vitro mutagenesis studies indicate that PTV and AMNV bind to the same pocket of the HP complex, probably engaging both helicase and primase subunits[19], both HPIs differ in their antiviral spectrum. Indeed, AMNV exhibits pan-α-herpesvirus coverage, whereas PTV antiviral activity is restricted to HSV-1 and HSV-2. Development of more potent broad-spectrum HPIs to treat α-herpesvirus infections and potentially other herpesviruses is challenging without understanding the exact binding mode and molecular mechanism of action of HPIs. Here, we present a high-resolution cryogenic electron microscopy (cryo-EM) structure of the HSV-1 HP complex and a detailed mapping of the binding sites of PTV and AMNV. Our findings provide structural insights into a novel molecular mechanism of action for antivirals, facilitating the future development of therapeutics targeting herpesviruses.

Results

Overall architecture of HSV-1 HP complex

The three HSV-1 HP subunits were purified as a stable heterotrimeric complex (Extended Data Fig. 2a–c). The purified complex was functional in unwinding double-stranded DNA, and could be inhibited by PTV and AMNV, with 50% inhibitory concentration (IC_{50}) values of 11.1 nM and 3.5 nM, respectively (Extended Data Fig. 2d–f). We determined the cryo-EM structures of the PTV- and AMNV-bound complex at near-atomic resolution (Fig. 1a, Extended Data Table 1 and Extended Data Fig. 3). In the two structures, the UL5 helicase features the characteristic seven conserved motifs of an SF1 helicase. UL8 adopts a canonical DNA polymerase-like fold with three subdomains: fingers, palm and thumb. The thumb specifically interacts with the AEP domain of UL52. The UL52 primase forms an elongated, arc-like structure ~130 Å in length, with the AEP domain and an N-terminal domain located at opposite ends, connected by a helical bundle (Extended Data Fig. 1b–d). This arrangement serves as a scaffold, producing a large surface that can wrap around UL5. The putative zinc-finger motif at the C terminus of UL52, proposed to bind DNA[12,13], is not resolved in the structure, probably owing to its inherent flexibility.

The HPI binding pocket

The density maps revealed that despite their chemical divergence, PTV and AMNV bind to the same pocket within the complex. AMNV adopts a Y-shaped conformation, whereas PTV is more extended (Figs. 1b,c and 2a). This pocket is enclosed by the UL52 α13 and α32 helices, the UL5 α17 helix and the UL5 motif IV loop. Polar interactions play a major role in anchoring both compounds, particularly between UL5 K356 and the acetamide carboxyl oxygen of PTV or the amino-2-oxoethyl oxygen of AMNV (Fig. 2b,c). Substitutions such as HSV-1 UL5 K356N, HSV-2 UL5 K355N and VZV K350N (equivalent positions) reduced sensitivity to PTV and/or AMNV by 200 to >2,000-fold[20,21], whereas a more limited decrease in potency (8–130-fold) has been reported for HSV-1 UL5 K356Q/T and HSV-2 UL5 K355E/R variants[21–23] (Extended Data Table 2). The greater potency loss from the K-to-N substitution may stem from the asparagine side chain being too short for direct interaction with the HPI acetamide oxygen but too long for water-mediated contacts. Structural analysis showed that HSV-1 UL5 residues N98 and N343 interact with the pyridine nitrogen of PTV and the 2,4-oxadiazole nitrogen of PTV (Fig. 2b,c). UL5 E359 forms an additional polar interaction with the oxadiazole oxygen of AMNV (Fig. 2c). Interestingly, an N342K substitution reduces the potency of PTV (≈40-fold)[24] and AMNV (≈600-fold for VZV N336K)[25] (Extended Data Table 2). Structural modelling indicates that the N342K substitution may clash with Y882, disrupting the interaction between N343 and PTV or directly

https://doi.org/10.1038/s41564-025-02168-4

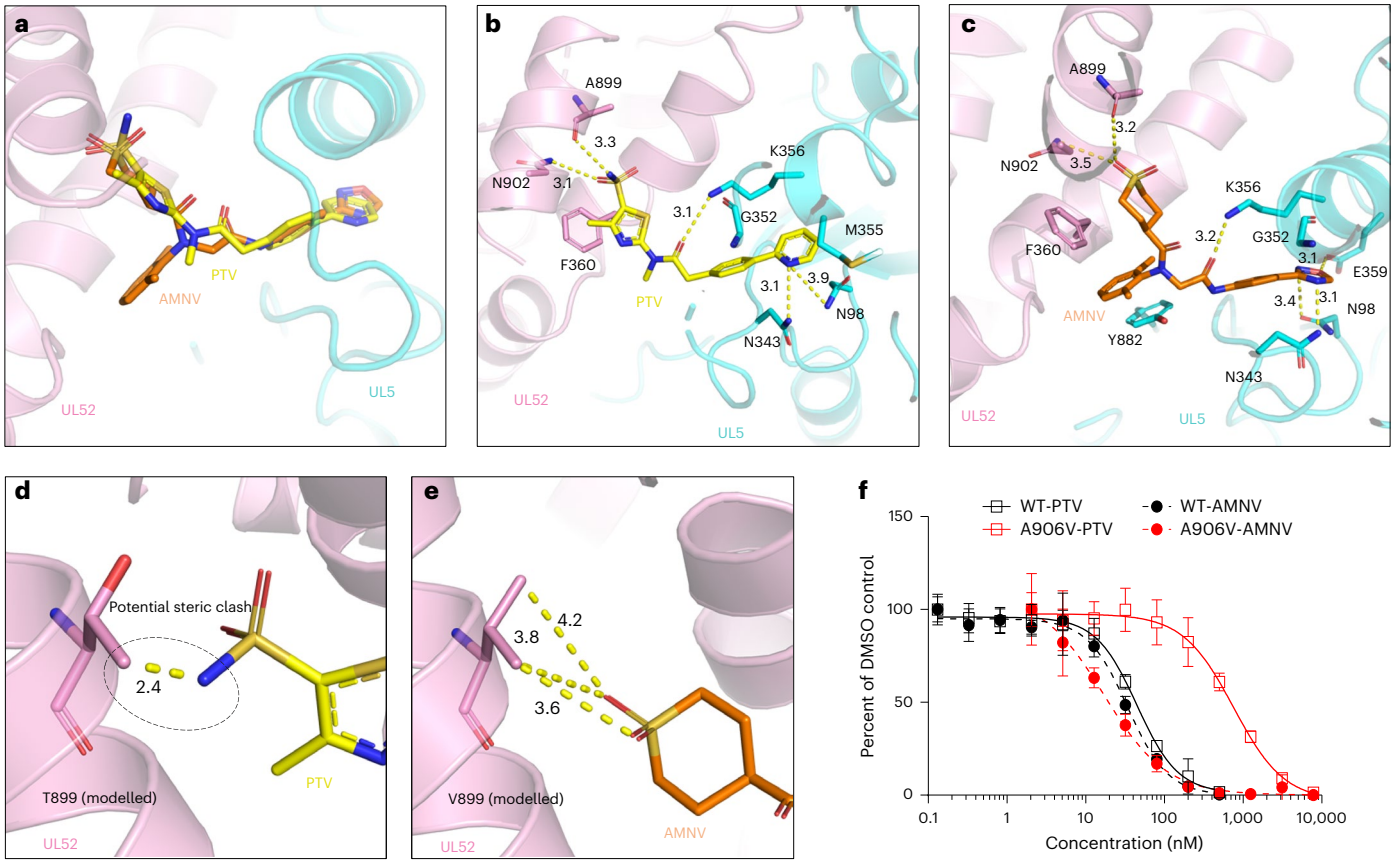

Fig. 2 | Detailed mapping of the HPI binding pocket between HSV-1 UL5 and UL52. a, Superimposition of the AMNV and PTV binding sites, using Cα atoms from both structures as reference points. AMNV and PTV are shown as stick models. **b**,**c**, Close-up views of the PTV (**b**) and AMNV (**c**) binding sites, with interaction residues (UL52 F306, A899, N902, UL5 N98, N343, K356, E359 and Y882) shown as sticks. Resistance mutant residues that form van der Waals interactions (G352 and M355) are also shown as sticks. Polar interactions are represented by yellow dashed lines, with numbers indicating approximate distances in Å. **d**,**e**, Proposed models explaining the PTV resistance associated with the HSV-1 UL52 A899T (and the HSV-2 UL52 A906V) substitution and the susceptibility of the VZV HP complex to AMNV (a valine is located at the equivalent position of UL52 A899 in VZV). The models show the most favourable rotamers for A899T (**d**) and A899V (**e**), with distances in Å between the side chains of the modelled threonine and valine residues to the PTV sulfonamide and AMNV sulfone head, respectively. **f**, Inhibition of viral DNA replication by PTV (solid) and AMNV (dotted) in ARPE-19 cells infected with HSV-2 WT (black) or a UL52 A906V variant (red). Representative dose–response curves from $n = 3$ independent biological replicates. Data are mean ± standard deviation from six replicates per condition.

interfering with PTV binding (Extended Data Fig. 4a,b). The reported reduced sensitivity of substitutions (V, R and C) at HSV-1 UL5 G352 and HSV-2 UL5 G351 (refs. 21,23,26) can be attributed to steric clashes with either ligand (Fig. 2b,c and Extended Data Table 2).

The density maps show that the thiazole ring of PTV and tetrahydrothiopyran-1,1-dioxide ring of AMNV interact with UL52 F360 via π–π stacking. PTV sulfonamide and AMNV sulfone form hydrogen bonds with the main-chain carboxyl oxygen of UL52 A899 as well as the side chain of N902 (Fig. 2b,c). The 43-fold reduction in PTV potency associated with a UL52 A899T substitution[23] (Extended Data Table 2) is intriguing because PTV engages the α-carboxyl group of UL52 A899 and this interaction is not expected to be disrupted by the additional side-chain carbon of a threonine (or a valine) residue. However, modelling suggested the most favourable A899T rotamer (90% probability) clashes with the sulfonamide of PTV (Fig. 2d), but not the tetrahydrothiopyran-1,1-dioxide ring of AMNV (Fig. 2e), predicting that AMNV would remain effective against A899T/V. Consistent with the predicted rotamer model, an HSV-2 A906V variant (equivalent position) remained fully sensitive to AMNV, while the 50% effective concentration (EC_{50}) of PTV shifted by 17-fold (Fig. 2f).

Specific to the HP-AMNV structure, the 2,6-dimethylphenyl ring of AMNV is inserted into a hydrophobic binding pocket composed of UL5 Y882, UL52 F360 and F907, engaging in hydrophobic interactions and a π–π stacking interaction with UL5 Y882 (Fig. 2c and Supplementary Fig. 1a). This AMNV arm is positioned at ~120° relative to the other arm, the tetrahydrothiopyran-1,1-dioxide ring, which occupies a cavity surrounded by UL5 H349, UL52 Y356, F360, N902, E905 and F907 (Supplementary Fig. 1b). In line with these findings, loss of sensitivity to AMNV was previously reported for UL52 variants bearing F360V/C (160-fold/25-fold) or N902T (9-fold) substitutions[21]. Indeed, the structural data predict that substituting F360 with smaller residues such as V or C would diminish or eliminate hydrophobic interactions formed by both the 2,6-dimethylphenyl and the tetrahydrothiopyran-1,1-dioxide rings of AMNV. These data also predict that a N902T substitution would weaken or abolish the hydrogen bond that coordinates the sulfone group of AMNV.

In vitro resistance to PTV

We performed dose-escalation resistance studies for PTV with both HSV-1 and HSV-2 to obtain additional functional data in support of our structural model. In the HSV-1 dose-escalation study, emergence of the UL5 K356N variant was observed (Extended Data Fig. 5a). This substitution conferred a substantial loss of sensitivity to PTV (210-fold) when introduced into a recombinant HSV-2 virus (UL5 K355N; Extended Data Fig. 5b and Extended Data Table 2). In the HSV-2

https://doi.org/10.1038/s41564-025-02168-4

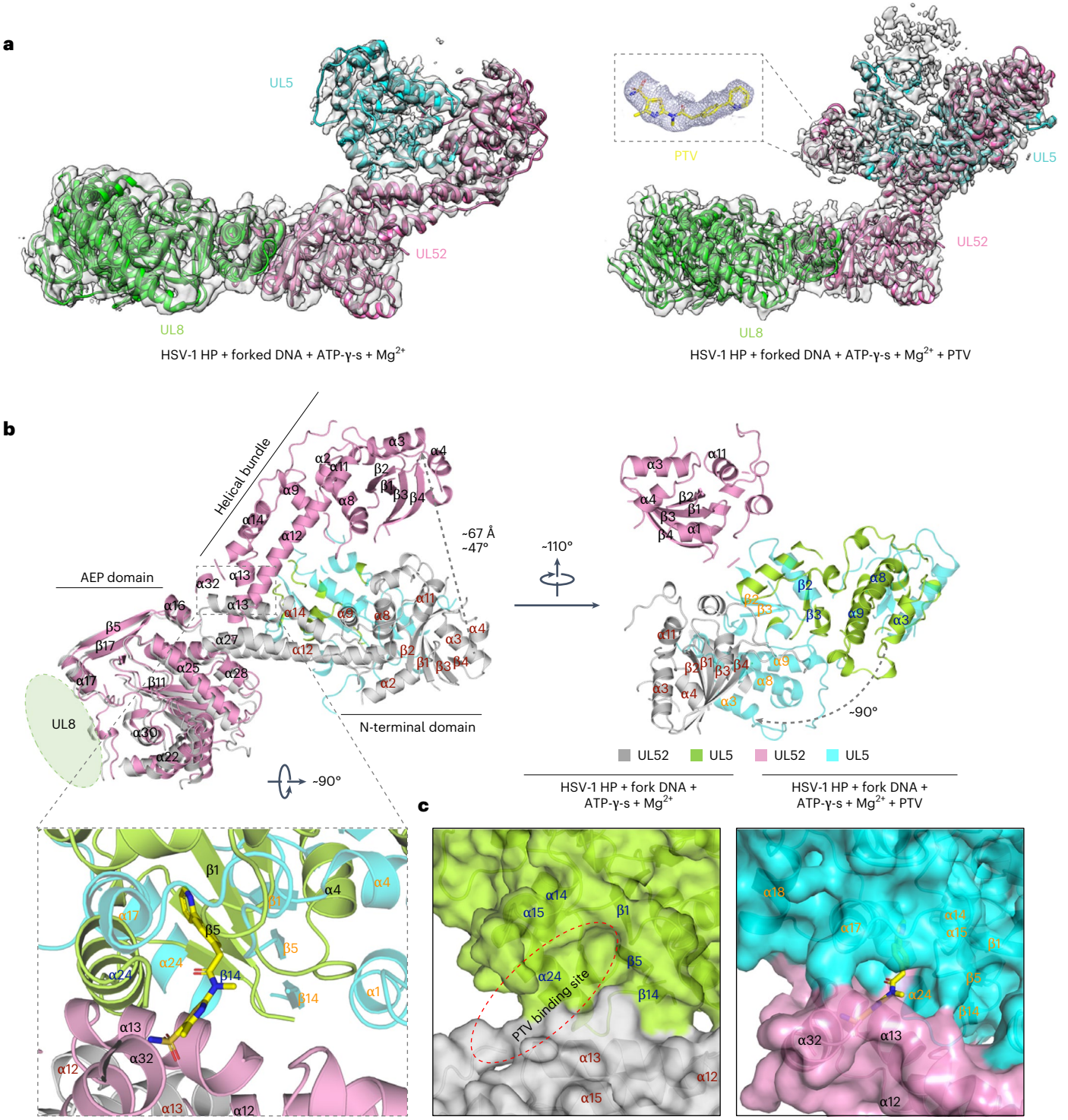

Fig. 3 | Structural changes induced by HPIs in HSV-1 UL5. a, Cryo-EM reconstructions of the PTV-free (left) and PTV-bound (right) HSV-1 HP complex with added substrates (forked DNA, ATP-γ-S and magnesium ion). Composite density maps are displayed in transparent grey, with atomic models shown as ribbon diagrams. In the PTV-bound structure, PTV is represented as sticks within a meshed density map contoured at 1.0σ. **b**, Top: comparison of conformational changes between the PTV-free and PTV-bound structures. Superimposition was based on the rigid region of the complex. For clarity, the UL8 structure is not shown, and secondary structure elements of UL52 and UL5 are numbered from the N to C terminus. Bottom: expanded view of the PTV binding site, with PTV shown as sticks. Structures are colour-coded as indicated on the right. **c**, Surface representations of the PTV-free and PTV-bound structures at the PTV binding site. Protein surfaces are shown with transparency and are coloured as in **b**, with PTV depicted as yellow sticks.

dose-escalation studies, a UL5 K355R variant was detected, either alone or paired with two additional substitutions, UL5 L805I and UL52 A906V (Extended Data Fig. 5a). UL5 L805I is ~25 Å away from the PTV binding site and is not expected to directly impact ligand binding. By contrast, UL52 A906 (equivalent to HSV-1 A899) stabilizes the PTV sulfonamide head (Fig. 2b), and an A-to-V substitution was associated with a 17-fold decrease in sensitivity to PTV (Fig. 2f). Strikingly, a recombinant HSV-2 virus bearing all three substitutions (UL5 K355R, L805I and UL52 A906V) was virtually insensitive to PTV (EC_{50} change >1,300-fold) (Extended Data Fig. 5b and Extended Data Table 2).

Mechanism of action of HPIs

To elucidate the molecular mechanism of action of HPIs, we attempted to determine the cryo-EM structures of the HSV-1 HP complex bound to forked DNA and ATP-γ-S, with and without PTV (Extended Data Table 1). The PTV-bound sample produced a well-resolved PTV density but lacked DNA and ATP-γ-S densities, resembling the substrate-free HSV-1 HP complex bound to PTV with minimal conformational changes (Fig. 3a). The PTV-free sample with substrates produced an intermediate-resolution map of the flexible region, with more unresolved regions predominantly located at the periphery, allowing for identification of secondary structure elements and docking of the UL5 and UL52 structures. However, side chains are not well resolved, and there are no densities for the DNA or ATP-γ-S. Nevertheless, a structural comparison with and without PTV revealed significant rotational motions in the helical bundle and N-terminal domain (~47°) of UL52 and in UL5 (~90°) around two nearly perpendicular axes converging near the PTV binding site (Fig. 3b). These motions stabilize UL52 α32 and UL5 motif IV and α17 by facilitating polar contacts and a π-stacking interaction, which are unresolved without PTV. Furthermore, UL5 undergoes an additional ~90° rotation along an axis nearly parallel to the helical bundle and positioned close to the PTV binding site, aligning its α17 and motif IV to engage with the acetamide linker and pyridine tail of PTV. This stabilizes UL52 α32 and UL5 motif IV and α17, which are also unresolved without PTV (Fig. 3b). These substantial conformational rearrangements create a cryptic cavity at the UL52–UL5 interface, where the head and tail of PTV deeply embed, leaving the acetamide linker partially solvent exposed (Fig. 3c).

SF1 helicases, such as Pif1, uvrD and RecD2, share a conserved core of seven motifs (Extended Data Fig. 6a and Supplementary Fig. 2), facilitating nucleotide binding and hydrolysis despite notable differences in their overall shapes and sequences[14]. Superimposing the HSV-1 UL5 core with those of other SF1 helicases revealed nearly identical motif positioning (Extended Data Fig. 6b), which enabled the single-stranded DNA (ssDNA) and adeonsine-5′-(β,γ-imido)triphosphate (ADPNP) grafting onto the UL5-PTV structure[27] (Fig. 4a). As an SF1B helicase, UL5-bound DNA runs in the 5′-3′ direction along an open groove that spans the top of the 2A domain and then traverses the 1A domain, similar to RecD2, positioning the unwound DNA near the UL52 catalytic site. The modelled ADPNP occupies the UL5 nucleotide binding site, which resembles the nucleotide-binding arrangement in other SF1 helicases (Extended Data Fig. 6). Notably, the ADPNP lies near the PTV binding site, separated by the UL5 motif IV loop, which adopts a conformation similar to the RecD2 ADPNP-bound motif IV loop. This loop engages with both ligands on opposite sides (Fig. 4a): R345 interacts with the β- and γ-phosphates of ADPNP, resembling the arginine finger found in RecD2, ATPases, GTPases and RecQ helicases[28–30], while adjacent N343 forms a hydrogen bond with the pyridine nitrogen of PTV (Figs. 2a and 4a). The dual interactions of the UL5 motif IV loop suggest a non-competitive allosteric inhibition mechanism[31]. Indeed, PTV disrupted the ATP-driven DNA unwinding activity of HSV-1 HP without competing with DNA or ATP (Extended Data Fig. 7).

We further investigated the PTV- and AMNV-mediated inhibition mechanism by comparing the UL5-PTV structure (modelled with ADPNP) to RecD2 helicase structures bound to ssDNA in both substrate (ADPNP-bound) and product (ADPNP-free) states. As an SF1B helicase, UL5 shares highly conserved core motifs and four domains with RecD2, despite the 2B domain remaining largely unresolved owing to its flexibility and the 1B domain being less defined because of limited sequence homology (Fig. 4 and Supplementary Fig. 3). This resemblance suggests that UL5 may use a RecD2-like inchworm translocation mechanism[27]. In RecD2, ATP hydrolysis drives coordinated conformational changes in the 2A, 2B and 1A domains, with the most significant shifts near the nucleotide binding site. The ADPNP binding causes a substantial rearrangement in motif IV of domain 1A, including a 180° flip and a shift of R493 by ~20 Å (Fig. 4b). Motif IV probably undergoes oscillatory movements synchronized with the ATP hydrolysis cycle, driving the functional dynamics of the 1A domain. Moreover, in UL5, motif IV and R345 adopt nearly identical ATP-bound positions, suggesting analogous conformational changes. However, in the PTV-bound structure, a hydrogen bond between N343 and the pyridine of PTV restricts loop mobility, preventing the ATP-driven rearrangements. In addition, UL5 K356 on the α17 helix of the 1A domain forms a strong stabilizing hydrogen bond with the acetamide linker of PTV, preventing the half-helical pitch shift needed for ATP hydrolysis, analogous to the shift observed in the equivalent α16 helix of RecD2 (Fig. 4c). The UL5–AMNV complex shows comparable stabilization, with N98, N343 and K356 forming hydrogen bonds with the oxadiazole and amino-2-oxoethyl linker of AMNV, plus an extra bond from E359 (Supplementary Fig. 4). Collectively, these interactions restrict the dynamics of motif IV and the 1A domain, thereby inhibiting ATP-driven translocation (summarized schematically in Fig. 5).

Discussion

Although never confirmed experimentally, the reduced susceptibility to PTV and AMNV observed with HSV UL5 and/or UL52 variants suggested that these HPIs bind both subunits of the HP complex[14,32]. The cryo-EM data reported here not only confirm this model but also demonstrate that PTV and AMNV occupy the same pocket despite their structural difference. By contrast, it was previously proposed that the binding mode of HPIs from the BILS series might not involve the UL52 subunit because BILS 22 BS is insensitive to the HSV-1 UL52 A899T substitution[23]. BILS 22 BS and AMNV share a common amino-2-oxoethyl-N linker and feature two large, branched rings at their heads (Extended Data Fig. 8a). However, unlike AMNV, the cyclohexane ring of BILS 22 BS does not form polar interactions with UL52 A899, as it lacks the sulfonamide or sulfone moiety seen in PTV and AMNV, providing a structural rationale for the lack of susceptibility of BILS 22 BS to the A899T mutation (Extended Data Fig. 8b). The structural data also resolved a perceived disconnect between the reduced susceptibility of the HSV-1 UL5 N342K variant to PTV and the distant positioning of the residue as predicted by comparative modelling and in silico docking[24]. While it was proposed that PTV might inhibit the HP complex via steric/allosteric hindrance to the UL5-UL52 interaction, the cryo-EM findings revealed a simpler mechanistic rationale in which UL5 N342 is closely juxtaposed to PTV and an N-to-K substitution would directly interfere with the binding of PTV to the pocket or through disruption to the local structure. This reinforces the limitations of integrating biological data and in silico predictions when validated structural information is lacking.

Overall, the high-resolution mapping of the HPI binding pocket resolved by cryo-EM aligns remarkably well with the in vitro resistance data published over the past two decades. Notably, we confirmed the importance of these resistant variants, including the HSV-2 UL5 K355T clinical variant[33], by engineering individual substitutions (or combinations thereof) into recombinant HSV-2. Our study emphasizes that the acetamide carboxyl oxygen present in all known HPIs is crucial for interacting with HSV-2 UL5 K355, rendering them susceptible to the emergence of resistant variants at this position. Thus, the presence of substitutions at this position should be carefully monitored in current and future clinical trials. In this context, IM-250 and HN0037, two HPIs structurally similar to PTV, have recently been evaluated in phase I clinical trials[34,35] (Extended Data Fig. 8c). Modelling of IM-250 in the HPI pocket enabled the accommodation of its unique sulfoximine and difluorophenyl groups, revealing an additional interaction between the 5-fluoro substituent and UL5 E359 (Extended Data Fig. 8d).

So far, no HPI has been reported to be active against human β-herpesviruses (that is, cytomegalovirus (CMV), HHV-6A, HHV-6B and HHV-7) or γ-herpesviruses (that is, Epstein–Barr virus and Kaposi sarcoma-associated herpesvirus). Furthermore, only AMNV is confirmed to exhibit pan-α-herpesvirus spectrum (HSV-1, HSV-2 and VZV), as the antiviral activity reported for other HPIs appears limited to

https://doi.org/10.1038/s41564-025-02168-4

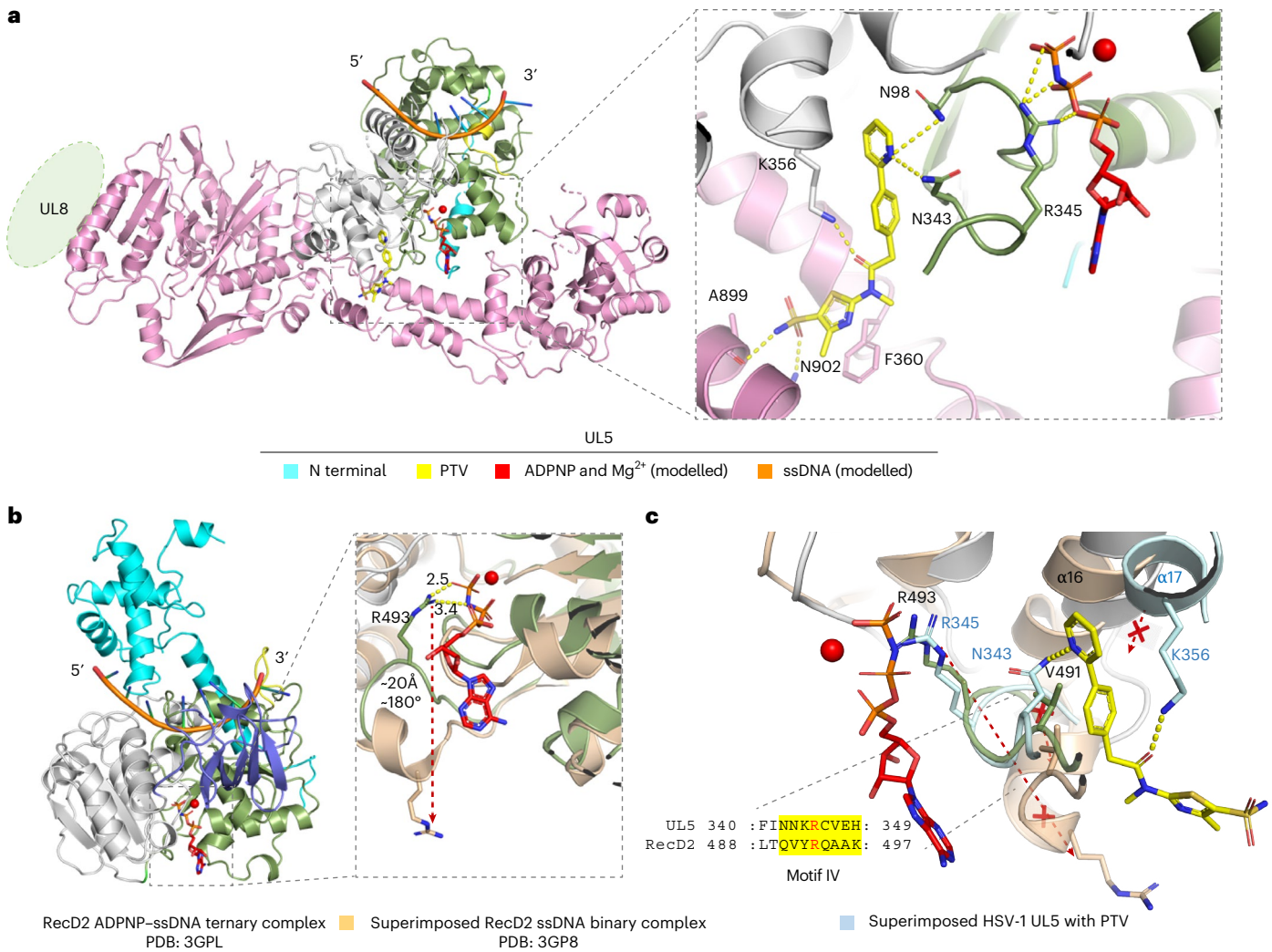

Fig. 4 | Molecular mechanism of action of HPIs on HSV-1 UL5 structure–function. a, Overall view of the PTV-bound HSV-1 HP complex with modelled DNA, ADPNP and Mg^{2+}. The complex is shown in a ribbon diagram, with the proposed UL5 domains (1A, green; 2A, grey; 2B, blue) derived from the sequence alignment shown in Supplementary Fig. 3. The colour scheme for other structural elements is indicated. The UL8 structure is omitted for clarity. PTV and ADPNP are represented as sticks, Mg^{2+} as a red sphere and DNA backbone is shown in orange, with the 5′ and 3′ ends labelled and individual bases depicted as single sticks. Right: an expanded view highlights the PTV and ADPNP binding sites, with potential polar interactions indicated by dashed lines. **b**, Conformational changes between the substrate and product states in RecD2. Left: the ribbon diagram shows the RecD2 substrate state, with ADPNP and DNA represented as in **a**. Right: an expanded view shows the ADPNP binding site in the substrate state superimposed with the product state. The arginine finger (R493) is shown as sticks, with interactions with ADPNP indicated by dashed lines, and conformational shifts in R493 and the motif IV loop are highlighted by a red arrow. **c**, Superimposition of the HP complex from **a** with the aligned RecD2 substrate and product states from **b** at the PTV and ADPNP binding sites. The superimposition is based on Cα atoms from the motif VI loop. Red arrows with a red cross show the inferred conformational changes in UL5 motif IV and α17 that are inhibited by PTV binding. The sequences of the motif IV loop from UL5 and RecD2 are aligned on the basis of the structural alignment, with the conserved arginine highlighted in red and motif IV residues shaded in yellow.

HSV-1 and HSV-2 (refs. 25,26,35–37). The structural mapping of the HPI binding pocket combined with an analysis of UL5/UL52 amino acid sequence conservation is key in deciphering the restricted antiviral spectrum of current HPIs. Indeed, a major HPI binding residue in HSV-1 not conserved in VZV is UL52 A899 (HSV-2 UL52 A906), which is instead a valine (ORF6 V936) (Supplementary Figs. 5 and 6). Remarkably, an A-to-V substitution at this position in HSV-2 conferred moderate resistance to PTV in vitro (17-fold) without affecting AMNV potency (Fig. 2f). Structurally, this is explained by the valine's preferential ligand-clashing rotamer, providing a molecular rationale for the narrow antiviral spectrum of PTV and analogous HPIs compared with AMNV. Nonetheless, considering that PTV is ~400-fold less potent against VZV than HSV-2 (Supplementary Fig. 7a,b), other structural features, which remain to be elucidated, also impair the ability of PTV to inhibit the VZV HP complex. A different structural rationale is at play for BILS 179 BS, which was reported to be 100 times more potent against HSV than VZV[25]. While structurally similar to AMNV (Extended Data Fig. 8a), this close analogue of BILS 22 BS does not engage A899 and thus should be fully compatible with a valine at the corresponding position in VZV. A structural analysis attributes the HSV-restricted spectrum of BILS 179 BS to its aminothiazole tail, which interacts favourably with M355 in HSV-1 UL5 but is less compatible with the isobutyl side chain of leucine 349 in VZV, the equivalent residue of UL5 M355 (Extended Data Fig. 8b). Thus, optimizing the aminothiazole tail of compounds from the BILS series could improve their activity against the VZV HP complex.

Broadening the spectrum of current HPI scaffolds to cover CMV appears particularly difficult owing to the lack of conservation of several HPI-binding residues in the CMV HP complex (Supplementary Figs. 5 and 6). Indeed, the crucial helicase residue HSV-1 UL5 N98 corresponds to CMV UL105 T144, which probably has a reduced affinity

https://doi.org/10.1038/s41564-025-02168-4

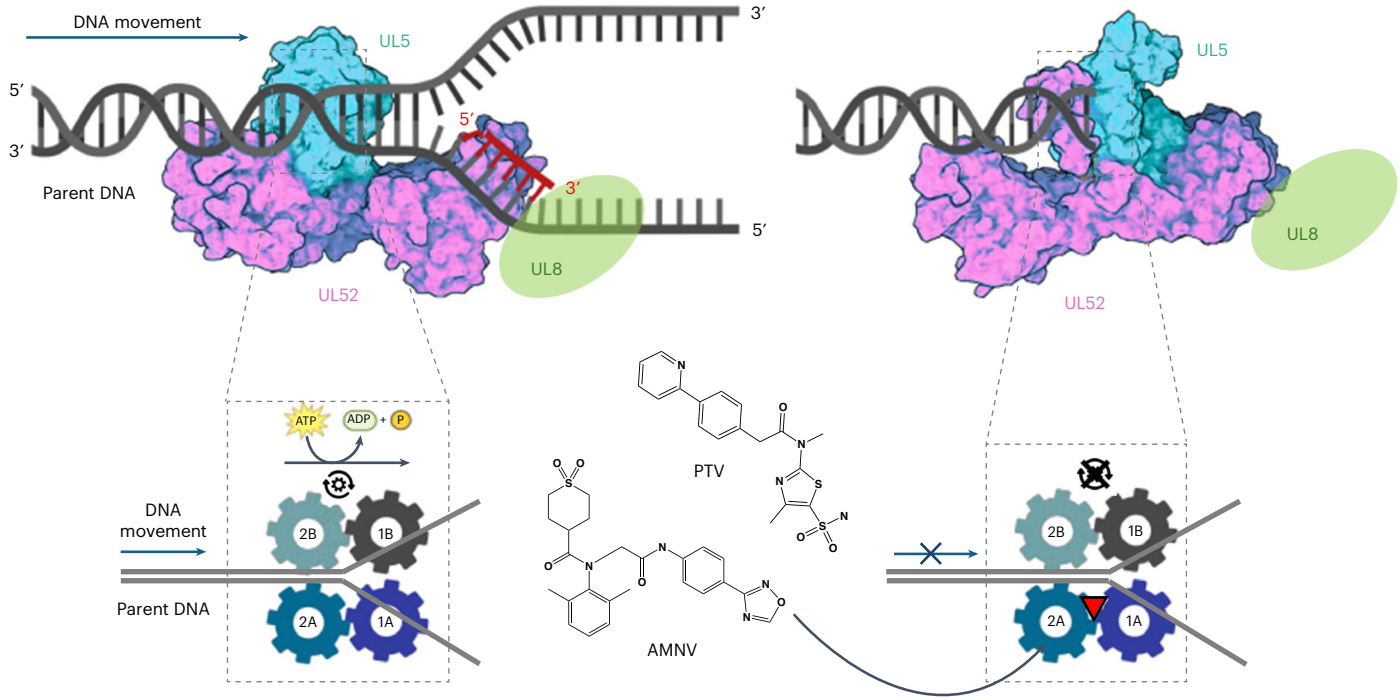

Fig. 5 | Schematic diagram illustrating the proposed mechanism of helicase inhibition by PTV and AMNV. The UL5 helicase (cyan) unwinds double-stranded parental DNA, separating it into two single strands (upper left). The UL52 primase (magenta) synthesizes RNA primers on the lagging strand in the 5′ to 3′ direction. UL5 and UL52 are shown in a surface representation to highlight structural changes when binding to PTV or AMNV; the UL8 accessory factor is denoted as a green oval. The four motor domains of the UL5 helicase are represented as rotating gears (lower left), which drive DNA translocation and strand separation using the energy derived from ATP hydrolysis. The chemical structures of PTV and AMNV are depicted (lower middle). Both function as molecular clogs by binding to the same allosteric site, obstructing the movement of the UL5 four motor domains that translocate and unwind double-stranded DNA, thereby inhibiting helicase activity (right). The forked lines denote that DNA translocation can either be blocked at an early stage (before unwinding is initiated) or halted at an intermediate state, where the two strands are unwound. Figure created with BioRender.com.

to the ligand. In addition, CMV UL105 H354, which is bulkier than its HSV-1 UL5 N342 equivalent, may sterically clash with F956, as shown Extended Data Fig. 4c. On the primase side, HSV-1 UL52 F360 is replaced with CMV UL70 R262, which would abrogate hydrophobic interactions with the ligand, while a CMV residue equivalent to HSV-1 UL52 A899 is simply absent. Altogether, these changes are incompatible with productive interactions between the CMV HP complex and PTV, AMNV or their analogues.

The concomitant inhibition of both helicase and primase activities has been demonstrated for multiple HPIs, underscoring the interdependence of UL5 and UL52 subunits in the HSV-1 HP complex[37,38]. The detection of HPI resistance mutations in both UL5 and UL52, and the reported stabilization of the HP complex by HPIs[37,39], has inferred that these inhibitors might lock the enzymatic complex in an inactive state. Our structural analysis showed that PTV and AMNV stabilize the HSV-1 HP complex in a conformation that blocks DNA translocation. In addition, as both PTV and AMNV interact with UL52 without directly compromising the structural integrity of its catalytic site, it is still unclear whether their binding stabilizes the complex in a manner that also allosterically inhibits primase activity. Future studies clarifying this mechanism would be valuable for developing more effective compounds that target the viral helicase, primase or both.

Finally, this study has several limitations. The flexible nature of the UL52 helical bundle, N-terminal domain and UL5, especially in the PTV-free sample, reduced the reconstruction quality, leaving features such as the zinc finger and certain peripheral elements blurred or unresolved. The ATP-γ-S and forked DNA densities were also not visible, possibly owing to limited occupancy or absence in the complex or limitations in heterogeneous reconstruction. In addition, the unsuccessful attempt to solve the ligand- and substrate-free form is probably due to more pronounced heterogeneity without stabilization by substrates or ligands. Therefore, the model of HSV-1 HP with PTV/AMNV, ssDNA, ADPNP and magnesium ion, built by template-based modelling, requires experimental validation. The proposed conformational changes in the UL5 1 A domain and motif IV loop, suggested by structural analysis and comparison, also need experimental confirmation.

Methods

Expression and purification of HSV-1 HP complex

Codon-optimized nucleotide sequences encoding HSV-1 helicase (UL5/UniProt ID P10189) and HP-associated protein (UL8/UniProt ID P10192) were cloned into the pFastBac-1 vector in frame with Flag and 8×-His tag, respectively. An untagged HSV-1 primase gene (UL52/UniProt ID P10236) was also cloned into the pFastBac-1 vector. Baculoviruses were generated in SF9 cells as per the manufacturer's instructions (Thermo Fisher Scientific). For protein expression, SF21 cells were co-infected with UL5, UL52 and UL8 baculoviruses at a multiplicity of infection (MOI) of 1:4:4, respectively. A total of 48 h after infection, cells were collected and stored at −80 °C. For protein purification, the cell pellet was resuspended in Buffer A (100 mM HEPES (pH 7.5), 150 mM NaCl, 5% glycerol) supplemented with Complete Protease Inhibitor (Roche). The cell suspension was passed through a microfluidics high-pressure homogenizer and the lysate was centrifuged at 29,819*g* for 60 min at 4 °C. The supernatant was collected and passed over a column packed with Anti-Flag G1 resin (Genscript). The column was washed with Buffer A and the target protein complex was eluted using Buffer B (100 mM HEPES (pH 7.5), 150 mM NaCl, 5% glycerol, 200 ng 3× Flag peptide per µl). The eluted sample was subsequently loaded over a HiLoad 16/600 Superdex 200 pg column equilibrated with Buffer C (50 mM Tris-HCl (pH 8.0), 500 mM NaCl, 5% glycerol). High-purity fractions were then pooled and passed over a Hi-Trap His FF column (Cytiva)

equilibrated with Buffer C and eluted with Buffer D (50 mM Tris-HCl (pH 8.0), 500 mM NaCl, 5% glycerol, 500 mM imidazole). The final protein preparation was dialysed and stored in Buffer D without imidazole. Analytical size-exclusion chromatography coupled with size-exclusion chromatography–high-performance liquid chromatography experiments were carried out by loading 15 µg purified protein complex over a Superose 6 Increase 5/150 GL column equilibrated with Buffer D using the 1260 Infinity II system (Agilent). Protein preparations of equivalent purity and activity were subsequently produced with the size exclusion chromatography step performed last.

Biochemical DNA unwinding assay

The DNA forked substrate was assembled by annealing an oligonucleotide labelled with a Cy5 fluorophore (5′-Cy5-GCACTGGCCGTCGTTTTACGGTCGTGACTGGGAAAACCCTGGCG-3′) (IDT) and another one labelled with a blackhole quencher BHQ3 (5′-TTTTTTTTTTTTTTTTTTTTTTTTCCAAGTAAAACGACGGCCAGTGC-BHQ3-3′) (IDT) at a respective molar ratio of 1:1.2. It was performed in annealing buffer (20 mM Tris (pH 8.0), 100 mM NaCl and 2 mM EDTA) by heating the samples at 95 °C for 8 min and slowly cooling them down to room temperature. A DNA trapping strand (5′-GCACTGGCCGTCGTTTTAC-3′) was used to capture unwound BHQ3 oligonucleotide strands and prevent re-annealing of the DNA forked substrate.

PTV and AMNV were custom-synthesized by Aragen and Santai Labs, respectively. Decreasing concentrations of either compounds in DMSO (ten-point, threefold dilution in quadruplicates) were spotted on black 384-well Optiplates (Perkin Elmer) using an ECHO acoustic dispenser, for a final concentration of DMSO of 0.5%. A total of 150 nM forked DNA substrate was incubated with 1 nM recombinant HSV-1 HP in unwinding assay buffer (20 mM Tris-HCl (pH 7.5), 1 mM DTT, 0.01% BSA, 0.01% Triton X-100, 5% glycerol and 5 mM $MgCl_2$). The reaction was initiated with the addition of 3 mM ATP (Promega) and 3.75 µM trap DNA (Sigma). All concentrations are final. After 24 h of incubation at room temperature, fluorescence was measured on an Envision plate reader (Perkin Elmer). Data were normalized to positive (PTV, 0% activity) and negative (vehicle, 100% activity) controls.

The ability of PTV to compete with DNA binding to the HSV-1 HP complex was tested in a DNA unwinding assay using 3 mM ATP and various concentrations of DNA and PTV. The ability of PTV to compete with ATP binding to the HSV-1 HP complex was tested using 150 nM DNA fork at various concentrations of ATP and PTV. The initial linear rates as a function of DNA/ATP and PTV concentrations were fit globally in GraphPad Prism using a mixed inhibition model to calculate the α factors and determine the mechanism of inhibition ($\alpha > 1$ is competitive, $\alpha \approx 1$ is non-competitive and $\alpha < 1$ is uncompetitive).

Cryo-EM sample preparation and data collection

Cryo-EM sample grids were prepared using a Vitrobot Mark IV system (Thermo Fisher Scientific). For grid preparation, 1.2 mg ml^{-1} of the HSV-1 HP complex with AMNV/PTV at a 1:10 molar ratio was diluted in a buffer containing 20 mM Tris-HCl (pH 7.4), 150 mM NaCl, 2.5% glycerol, 1 mM tris(2-carboxyethyl)phosphine and 0.04 mM dodecylmaltoside. For samples containing substrates, additional components included 5 mM $MgCl_2$, forked DNA at a 4:1 molar ratio to the HP complex and ATP-γ-S (Roche) at a 10:1 molar ratio, with or without PTV. The forked DNA was prepared following the sequences and protocol of the DNA substrate used in the unwinding assay, with the Cy5 and BHQ3 labels removed. The sample solutions were applied to glow-discharged UltraAuFoil grids (300 Mesh, R1.2/1.3, Quantifoil) inside the Vitrobot chamber, maintained at 4 °C and ≥95% relative humidity. Each grid was blotted with filter paper (TED Pella) for 2.5 s before being plunged into liquid ethane using a force setting of 0 and a 10-s wait time. The GO grid sample preparation used two types of grids: commercially available GraFuture grids (Shuimu Biosciences) and homemade grids prepared according to the protocol described[40]. Each grid was blotted for 4.5 s using a force setting of 0 and a 30-s wait time.

Micrographs were collected on a Krios G4 microscope (Thermo Fisher Scientific) with a cold field emission gun operating at 300 kV, equipped with a Selectris-X energy filter and Falcon 4i direct electron detector. Data acquisition was operated using EPU software (Thermo Fisher Scientific) at a nominal magnification of 165,000×, resulting in a pixel size of 0.729 Å. Defocus values were set between −0.6 µm and −2.2 µm, with a total electron dose of ~50 e^{-} $Å^{-2}$, fractionated evenly across 50 frames.

Cryo-EM image processing and model building

A summary of the major steps in processing data for the HSV-1 HP complex with AMNV is shown in Extended Data Fig. 3. Motion correction and contrast transfer function (CTF) estimation were performed using CryoSPARC's Patch Motion Correction and Patch CTF[41]. Micrographs with CTF resolution better than 3.6 Å and a relative thickness below 1.09 were selected for further analysis. Multiple rounds of autopicking were tested using CryoSPARC's blob and template pickers to optimize parameters. Duplicate particles were removed before two-dimensional (2D) classification, and high-quality class particles were extracted and refined through iterative 2D classifications and subset selections. Particles from selected high-quality 2D classes were used to generate a de novo initial model, followed by a consensus three-dimensional refinement using CryoSPARC's non-uniform refinement[42].

The UCSF PyEM package[43] was used to convert CryoSPARC particles into a format compatible with Relion[44]. Masks for each body were generated using the relion_mask_create command. Relion 5.0 multi-body refinement with Blush regularization was used to independently refine the rigid and flexible parts and integrating them into a high-resolution composite map[44,45]. The final Fourier shell correlation (FSC) curves were calculated in Relion 5.0, and the resolutions were assessed using the 0.143 FSC criterion. The final raw maps were subsequently sharpened using DeepEMhancer for model building[46]. AlphaFold-predicted models of UL8, UL5 and UL52 served as initial templates for rigid body docking[47]. Each protein structure was docked into enhanced EM maps using UCSF Chimera[48]. After orientation determination, the models were manually built and adjusted in Coot[49] and refined with Phenix.real_space_refine[50]. The UL52 A899T, A899V and UL5 N342K mutations were modelled in UCSF Chimera, with rotamer probabilities calculated using the Dunbrack 2010 rotamer library[51]. Other simple mutations were modelled using the Simple Mutation function in Coot[49]. Figures were then generated using UCSF Chimera and PyMOL (https://pymol.org/).

Dose-escalation resistance

Vero cells (ATCC) were seeded at a density of 400,000 cells per well in tissue culture 12-well plates (Corning) and incubated at 37 °C overnight. Cells were then infected with HSV-1 MS or HSV-2 KOS virus at MOI 0.2 for 2 h. PTV was added to the plate at concentrations equivalent to 0.5× EC_{50} (HSV-2 EC_{50} 11.8 nM, HSV-1 EC_{50} 6.6 nM) and increased by fourfold when full cytopathic effect (CPE) was observed. If CPE was not observed after 2 weeks in culture, twofold increases were performed instead. Virus populations in each passage were tittered and used to initiate a new infection at a constant MOI of 0.2 until a 'maximum' concentration was achieved, that is, a concentration which when doubled did not result in detectable CPE after 2 weeks in cell culture.

DNA was extracted from collected supernatants using QIAamp DNA Blood Mini Kit (Qiagen) and quantified by nanodrop (Thermo Fisher Scientific). Amplicons for UL5 and UL52 were generated by polymerase chain reaction (PCR) amplification using Platinum SuperFi II DNA Polymerase (Thermo Fisher Scientific) and sent to Novogene for library construction using Rapid Plus DNA Library Prep Kit (ABclonal). Libraries were quantified using Qubit and their size distribution was assessed by bioanalyser. Whole genome sequencing was performed on NovaSeq 6000 S4 (Illumina).

Generation and phenotyping of HSV-2 recombinant mutants

Six single mutants (UL5 K355N, K355R, K355T, L805I and S497N; UL52 A906V) and two double mutants (UL5 K355N/S497N and K355R/L805I) were generated in an HSV-2 bacterial artificial chromosome (BAC) system using en passant mutagenesis[52]. The BAC encoding MS strain HSV-2 with an mCherry reporter (GenBank accession no. MH796783.1)[53], used in the generation of all recombinant HSV-2 mutant viruses, was kindly provided by Dr Viejo-Borbolla (Hannover Medical School). In brief, a recombination template encoding the desired mutation(s), a Kan-resistance cassette, and I-SceI endonuclease was generated by PCR and electroporated into recombination-competent GS1783 *Escherichia coli* cells (licensed from Northwestern University). KanR colonies were screened by colony PCR for candidate mutant BACs. Candidate BACs were then subjected to a second round of recombination along with I-SceI induction to generate scarless mutant BACs, which were confirmed via restriction digest and Sanger sequencing. Successfully generated BACs were kept in long-term storage as glycerol stocks. All BAC purifications were performed with the NucleoBond Xtra BAC purification kit (Macherey-Nagel). Single mutant viruses were rescued by transfecting purified BACDNA into 293FT cells (ThermoFisher) using TransIT-LT1 (Mirus Bio) and subsequently used to infect Vero cells for bulk virus propagation. Cellular mCherry expression was measured to titre recombinant viruses.

ARPE-19 cells (ATCC) cultured in growth medium (DMEM/F-12 with GlutaMAX, Thermo Fisher Scientific) with 10% foetal bovine serum (FBS) were briefly trypsinized and bulk infected with HSV-2 recombinant viruses at MOI 0.5 for 1 h shaking at room temperature. ARPE-19 cells were seeded at a density of 25,000 cells per well in black clear-bottom 96-well plates (Corning) and incubated at 37 °C for 1 h. PTV was added to the plate in 2.5- to 4-fold dilution series and normalized to a final concentration of 0.5% DMSO. Cells were stained with Hoechst dye and mCherry signal was quantified using Cellomics (Thermo Fisher Scientific) for EC_{50} determination 20 h after infection. Uninfected controls were used to minimize background signal.

HSV-2 and VZV antiviral assays

ARPE-19 cells were bulk infected with HSV-2 (MS strain) at MOI 0.5 in assay medium (growth medium with 2% FBS) for 1 h under rotation at room temperature. A total of 100 µl infected cells (25,000 cells) were added onto 96-well assay plates (Corning) that were pre-spotted with 500 nl of compounds serially diluted in DMSO using an HP Digital Dispenser D300 (Hewlett Packard). Plates were incubated at 37 °C for 20 h, after which cells were collected using a PrepGEM DNA extraction kit (MicroGEM) following the manufacturer's protocol. A cellular quantitative PCR (qPCR)-based assay was used to measure viral replication by quantifying UL30 (DNA polymerase) levels within the cell lysate. In brief, a qPCR master mix (Quantifast Multiplex kit, Qiagen) was prepared with HSV UL30-FAM primer/probe mix (HSV_UL30_F, 5′-AGAGGGACATCCAGGACTTTGT-3′; HSV_UL30_R, 5′-CAGGCGCTTGTTGGTGTAC-3′; HSV_UL30_FAM, 5′-/56-FAM/AC CGC CGA A/ZEN/C TGA GCA /3IABkFQ/-3′) (IDT) added to all samples, ran on a QuantStudio Real-time PCR machine (Thermo Fisher Scientific) at 95 °C for 5 min, 40 cycles of 95 °C for 30 s, and 60 °C for 30 s. Quantitative HSV-1/HSV-2 genomic DNA (ATCC) used as a standard curve and relative gene expression was calculated via comparative Ct values ($\Delta\Delta C_T$).

ARPE-19 cells (3×10^6) were seeded in a T75 flask and incubated in growth medium at 37 °C. The next day, 1 ml VZV Oka (ATCC VR-1832) was added, and, when ~20% CPE was observed (2–4 days later), cells were passaged at a ratio of 1:20 (infected:uninfected) and incubated for an additional 2 days. VZV-infected cells were then cryopreserved in assay-ready aliquots of 3×10^6 cells per vial. These aliquots were thawed in 12 ml assay medium, and 100 µl (25,000 cells) were added into wells of a 96-well assay plate pre-spotted with 500 nl of compounds serially diluted in DMSO. Assay plates were incubated at 37 °C for 3 days, after which VZV DNA replication was evaluated by qPCR as described above, except for the primer/probe mix (VZV_IE62_F (5′-CCTCCGTATCGGGACTTCAA-3′), VZV_IE62_R (5′-TGACCGTCCTCGCATACGTA-3′) and VZV_IE62_FAM (5′-/56-FAM/TTGGCGAAG/ZEN/AGCTAAC/3IABkFQ/-3′)).

Statistics and reproducibility

The sample sizes in this study (number of technical and biological replicates) were based on experience as data interpretation did not require analyses of statistical significance. All values derived from independent replicates are captured; no experiments were excluded. The experiments were not randomized. The investigators were not blinded to allocation during experiments and outcome assessments.

Reporting summary

Further information on research design is available in the Nature Portfolio Reporting Summary linked to this article.

Data availability

The cryo-EM density maps generated in this study have been deposited in the Electron Microscopy Data Bank under the following accession codes: EMDB-49269, EMDB-49326; EMDB-49304, EMDB-49306; EMDB-49290, EMDB-49291; and EMDB-49276, EMDB-49277. Each pair corresponds to the two bodies of the HSV-1 helicase–primase (HP) complex with amenamevir (AMNV), the HSV-1 HP complex with pritelivir (PTV), the HSV-1 HP complex prepared with DNA, ATP-γ-S, Mg^{2+} and PTV, and the HSV-1 HP complex prepared with DNA, ATP-γ-S and Mg^{2+}, respectively. The corresponding atomic coordinates for the structural models have been deposited in the Protein Data Bank under the following accession codes: 9NDA, 9NEL; 9NEB, 9NEE; 9NDZ, 9NE0; and 9NDQ, 9NDT, with each pair representing the two bodies of the respective complex. All other relevant data generated and analysed during this study are included in this Article and its Supplementary Information. Source data are provided with this paper.

References

1. Arvin, A. et al. *Human Herpesviruses: Biology, Therapy, and Immunoprophylaxis* (Cambridge Univ. Press, 2007).
2. Lee, D. H. & Zuckerman, R. A. Herpes simplex virus infections in solid organ transplantation: guidelines from the American Society of Transplantation Infectious Diseases Community of Practice. *Clin. Transplant.* **33**, e13526 (2019).
3. Pergam, S. A. & Limaye, A. P. Varicella zoster virus in solid organ transplantation: guidelines from the American Society of Transplantation Infectious Diseases Community of Practice. *Clin. Transpl.* **33**, e13622 (2019).
4. Itzhaki, R. F. et al. Herpes simplex virus type 1 in brain and risk of Alzheimer's disease. *Lancet* **349**, 241–244 (1997).
5. Taquet, M., Dercon, Q., Todd, J. A. & Harrison, P. J. The recombinant shingles vaccine is associated with lower risk of dementia. *Nat. Med.* https://doi.org/10.1038/s41591-024-03201-5 (2024).
6. Ou, Y. N. et al. Associations of infectious agents with Alzheimer's disease: a systematic review and meta-analysis. *J. Alzheimers Dis.* **75**, 299–309 (2020).
7. Chen, V. C. et al. Herpes zoster and dementia: a nationwide population-based cohort study. *J. Clin. Psychiatry* https://doi.org/10.4088/JCP.16m11312 (2018).
8. Mertz, G. J. Long-term acyclovir suppression of frequently recurring genital herpes simplex virus infection. *J. Am. Med. Assoc.* https://doi.org/10.1001/jama.1988.03410020067030 (1988).
9. Corey, L. et al. Once-daily valacyclovir to reduce the risk of transmission of genital herpes. *N. Engl. J. Med.* **350**, 11–20 (2004).

10. Schalkwijk, H. H., Snoeck, R. & Andrei, G. Acyclovir resistance in herpes simplex viruses: prevalence and therapeutic alternatives. *Biochem. Pharmacol.* **206**, 115322 (2022).
11. Byrd, A. K. & Raney, K. D. Structure and function of Pif1 helicase. *Biochem. Soc. Trans.* **45**, 1159–1171 (2017).
12. Taylor, A. F. & Smith, G. R. Monomeric RecBCD enzyme binds and unwinds DNA. *J. Biol. Chem.* **270**, 24451–24458 (1995).
13. Singleton, M. R., Dillingham, M. S. & Wigley, D. B. Structure and mechanism of helicases and nucleic acid translocases. *Annu. Rev. Biochem.* **76**, 23–50 (2007).
14. Bermek, O. & Williams, R. S. The three-component helicase/primase complex of herpes simplex virus-1. *Open Biol.* **11**, 210011 (2021).
15. Birkmann, A. & Saunders, R. Overview on the management of herpes simplex virus infections: current therapies and future directions. *Antivir. Res.* **237**, 106152 (2025).
16. *ClinicalTrial.gov* https://clinicaltrials.gov/study/NCT03073967 (2017).
17. Shoji, N. et al. Pharmaceuticals and Medical Device Agency approval summary: amenamevir for the treatment of herpes zoster. *J. Dermatol.* **47**, 683–688 (2020).
18. Maruho receives manufacturing and marketing approval for a partial change of the indication and dosage/administration for anti-herpes rirus agent "Amenalief Tab. 200mg" for the treatment of recurrent Herpes Simplex in Japan. *Maruho News* https://www.maruho.co.jp/english/information/20230224.html (2023).
19. Biswas, S., Sukla, S. & Field, H. J. Helicase–primase inhibitors for herpes simplex virus: looking to the future of non-nucleoside inhibitors for treating herpes virus infections. *Future Med. Chem.* **6**, 45–55 (2014).
20. Biswas, S., Smith, C. & Field, H. J. Detection of HSV-1 variants highly resistant to the helicase–primase inhibitor BAY 57-1293 at high frequency in 2 of 10 recent clinical isolates of HSV-1. *J. Antimicrob. Chemother.* **60**, 274–279 (2007).
21. Sato, Y. et al. Characteristics of helicase–primase inhibitor amenamevir-resistant herpes simplex virus. *Antimicrob. Agents Chemother.* **65**, e0049421 (2021).
22. Biswas, S., Jennens, L. & Field, H. J. Single amino acid substitutions in the HSV-1 helicase protein that confer resistance to the helicase–primase inhibitor BAY 57-1293 are associated with increased or decreased virus growth characteristics in tissue culture. *Arch. Virol.* **152**, 1489–1500 (2007).
23. Biswas, S. et al. A single drug-resistance mutation in HSV-1 UL52 primase points to a difference between two helicase–primase inhibitors in their mode of interaction with the antiviral target. *J. Antimicrob. Chemother.* **61**, 1044–1047 (2008).
24. Biswas, S., Miguel, R. N., Sukla, S. & Field, H. J. A mutation in helicase motif IV of herpes simplex virus type 1 UL5 that results in reduced growth in vitro and lower virulence in a murine infection model is related to the predicted helicase structure. *J. Gen. Virol.* **90**, 1937–1942 (2009).
25. Chono, K. et al. ASP2151, a novel helicase–primase inhibitor, possesses antiviral activity against varicella-zoster virus and herpes simplex virus types 1 and 2. *J. Antimicrob. Chemother.* **65**, 1733–1741 (2010).
26. Kleymann, G. et al. New helicase–primase inhibitors as drug candidates for the treatment of herpes simplex disease. *Nat. Med.* **8**, 392–398 (2002).
27. Saikrishnan, K., Powell, B., Cook, N. J., Webb, M. R. & Wigley, D. B. Mechanistic basis of 5′-3′ translocation in SF1B helicases. *Cell* **137**, 849–859 (2009).
28. Komoriya, Y. et al. Principal role of the arginine finger in rotary catalysis of F1-ATPase. *J. Biol. Chem.* **287**, 15134–15142 (2012).
29. Mann, D. et al. Mechanism of the intrinsic arginine finger in heterotrimeric G proteins. *Proc. Natl Acad. Sci. USA* **113**, E8041–E8050 (2016).
30. Ren, H. et al. The arginine finger of the Bloom syndrome protein: its structural organization and its role in energy coupling. *Nucleic Acids Res.* **35**, 6029–6041 (2007).
31. Strelow J. D. W. et al. in *Assay Guidance Manual* (ed. Grossman, A. et al.) 1–27 (NCATS, 2012).
32. Weller, S. K. & Kuchta, R. D. The DNA helicase–primase complex as a target for herpes viral infection. *Expert Opin. Ther. Targets* **17**, 1119–1132 (2013).
33. Spengler, J. R. et al. Meeting report: 35th International Conference on Antiviral Research in Seattle, Washington, USA - March 21–25, 2022. *Antivir. Res.* **211**, 105521 (2023).
34. *ClinicalTrials.gov* https://clinicaltrials.gov/study/NCT06435507 (2024).
35. Hou, J. et al. Pharmacokinetics and safety study of HN0037, a novel anti-human herpes simplex virus inhibitor, in healthy volunteers. *Clin. Pharmacol. Drug Dev.* https://doi.org/10.1002/cpdd.1138 (2022).
36. Gege, C. et al. A helicase–primase drug candidate with sufficient target tissue exposure affects latent neural herpes simplex virus infections. *Sci. Transl. Med.* https://doi.org/10.1126/scitranslmed.abf8668 (2021).
37. Crute, J. J. et al. Herpes simplex virus helicase–primase inhibitors are active in animal models of human disease. *Nat. Med.* **8**, 386–391 (2002).
38. Spector, F. C., Liang, L., Giordano, H., Sivaraja, M. & Peterson, M. G. Inhibition of herpes simplex virus replication by a 2-amino thiazole via interactions with the helicase component of the UL5–UL8–UL52 complex. *J. Virol.* **72**, 6979–6987 (1998).
39. Muylaert, I., Zhao, Z. & Elias, P. UL52 primase interactions in the herpes simplex virus 1 helicase–primase are affected by antiviral compounds and mutations causing drug resistance. *J. Biol. Chem.* **289**, 32583–32592 (2014).
40. Patel, A., Toso, D., Litvak, A. & Nogales, E. Efficient graphene oxide coating improves cryo-EM sample preparation and data collection from tilted grids. Preprint at *bioRxiv* https://doi.org/10.1101/2021.03.08.434344 (2021).
41. Punjani, A., Rubinstein, J. L., Fleet, D. J. & Brubaker, M. A. cryoSPARC: algorithms for rapid unsupervised cryo-EM structure determination. *Nat. Methods* **14**, 290–296 (2017).
42. Punjani, A., Zhang, H. & Fleet, D. J. Non-uniform refinement: adaptive regularization improves single-particle cryo-EM reconstruction. *Nat. Methods* **17**, 1214–1221 (2020).
43. Asarnow, D., Palovcak, E. & Cheng, Y. asarnow/pyem: UCSF pyem v0.5. *Zenodo* https://doi.org/10.5281/zenodo.3576629 (2019).
44. Scheres, S. H. RELION: implementation of a Bayesian approach to cryo-EM structure determination. *J. Struct. Biol.* **180**, 519–530 (2012).
45. Kimanius, D. et al. Data-driven regularization lowers the size barrier of cryo-EM structure determination. *Nat. Methods* **21**, 1216–1221 (2024).
46. Sanchez-Garcia, R. et al. DeepEMhancer: a deep learning solution for cryo-EM volume post-processing. *Commun. Biol.* **4**, 874 (2021).
47. Jumper, J. et al. Highly accurate protein structure prediction with AlphaFold. *Nature* **596**, 583–589 (2021).
48. Pettersen, E. F. et al. UCSF Chimera–A visualization system for exploratory research and analysis. *J. Comput. Chem.* **25**, 1605–1612 (2004).
49. Emsley, P. & Cowtan, K. Coot: model-building tools for molecular graphics. *Acta Crystallogr. D* **60**, 2126–2132 (2004).
50. Afonine, P. V. et al. Real-space refinement in PHENIX for cryo-EM and crystallography. *Acta Crystallogr D* **74**, 531–544 (2018).
51. Shapovalov, M. V. & Dunbrack, R. L. Jr. A smoothed backbone-dependent rotamer library for proteins derived from adaptive kernel density estimates and regressions. *Structure* **19**, 844–858 (2011).

52. Tischer, B. K., Smith, G. A. & Osterrieder, N. En passant mutagenesis: a two step markerless red recombination system. *Methods Mol. Biol.* **634**, 421–430 (2010).
53. Kropp, K. A. et al. Herpes simplex virus 2 counteracts neurite outgrowth repulsion during infection in a nerve growth factor-dependent manner. *J. Virol.* https://doi.org/10.1128/JVI.01370-20 (2020).
54. Harauz, G. & van Heel, M. Exact filters for general geometry three dimensional reconstruction. *Optik* **78**, 146–156 (1986).
55. Lu, K. Y. et al. Insights into the structural and mechanistic basis of multifunctional S. cerevisiae Pif1p helicase. *Nucleic Acids Res.* **46**, 1486–1500 (2018).
56. Lee, J. Y. & Yang, W. UvrD helicase unwinds DNA one base pair at a time by a two-part power stroke. *Cell* **127**, 1349–1360 (2006).
57. Effendi, G. B. et al. Single amino acid substitution within the helicase of varicella zoster virus makes it resistant to amenamevir. *J. Med. Virol.* **96**, e70080 (2024).
58. Chono, K., Katsumata, K., Kontani, T., Shiraki, K. & Suzuki, H. Characterization of virus strains resistant to the herpes virus helicase–primase inhibitor ASP2151 (amenamevir). *Biochem. Pharmacol.* **84**, 459–467 (2012).
59. Biswas, S., Swift, M. & Field, H. J. High frequency of spontaneous helicase–primase inhibitor (BAY 57–1293) drug-resistant variants in certain laboratory isolates of HSV-1. *Antivir. Chem. Chemother.* **18**, 111–112 (2007).

Acknowledgements

We thank J. Perry from the Structural Biology and Chemistry department and T. Stratton from the Medicinal Chemistry department for their advice and helpful discussions. We also thank D. Mortenson from the Structural Biology and Chemistry department, as well as M. M. Holdorf and S. P. Fletcher from the Virology department for their thorough review of the paper. Moreover, we thank the members of the Medicinal Chemistry, Structural Biology and Chemistry and Discovery Virology departments at Gilead Sciences, Inc., for their helpful discussions and technical assistance. This work was funded by Gilead Sciences, Inc. The funder had no role in the study design, data collection or analysis, decision to publish or paper preparation. Before submission, the funder reviewed the paper to ensure compliance with proprietary data management policies and granted approval for publication.

Author contributions

Q.Y. conducted cryogenic electron microscopy (cryo-EM) experiments and analysed the cryo-EM structures with the assistance from X.Y. A.N. designed expression vectors, established the recombinant protein purification protocol and purified recombinant proteins. A.L.-B. and A.S. developed and performed the biochemical helicase assays. V.N. performed herpes simplex virus type 2 (HSV-2) and varicella zoster virus (VZV) antiviral assays. R.M. designed and L.M. performed dose-escalation resistance studies. P.Y.H. generated next-generation sequencing data that were analysed by T.A. C.R. designed the HSV variants that were phenotyped by L.M. and P.Y.H. J.M. helped with modelling simulations. A.M. coordinated biology activities, assisted with biology data analysis and supervised V.N. A.C. initiated the structural chemistry efforts, and E.L. provided general project oversight. Q.Y. and A.M. wrote the paper with input from all authors.

Competing interests

All authors are current employees of Gilead Sciences, Inc. and received salary and stock ownership as compensation for their employment.

Additional information

Extended data is available for this paper at https://doi.org/10.1038/s41564-025-02168-4.

Supplementary information The online version contains supplementary material available at https://doi.org/10.1038/s41564-025-02168-4.

Correspondence and requests for materials should be addressed to Qing Yao or Alexandre Mercier.

Reviewer recognition *Nature Microbiology* thanks the anonymous reviewer(s) for their contribution to the peer review of this work. Peer reviewer reports are available.

https://doi.org/10.1038/s41564-025-02168-4

Extended Data Table 1 | Cryo-EM data collection, refinement, and validation statistics for the HSV-1 HP complex structures presented in this study

	HP+AMNV		HP+PTV		HP+PTV+forked DNA+ATP-γ-S+Mg^{2+}		HP+forked DNA+ATP-γ-S+Mg^{2+}	
EMDB ID	Body1 EMD-49269	Body2 EMD-49326	Body1 EMD-49304	Body2 EMD-49306	Body1 EMD-49290	Body2 EMD-49291	Body1 EMD-49276	Body2 EMD-49277
PDB ID	9NDA	9NEL	9NEB	9NEE	9NDZ	9NEO	9NDQ	9NDT
Data collection and processing								
Magnification	165,000	165,000	165,000	165,000	165,000	165,000	165,000	165, 000
Voltage (kV)	300	300	300	300	300	300	300	300
Electron exposure (e–/Å^2)	50	50	50	50	50	50	50	50
Defocus range (μm)	-0.6 to -2.2	-0.6 to -2.2	-0.6 to -2.2	-0.6 to -2.2	-0.6 to -2.2	-0.6 to -2.2	-0.6 to -2.2	-0.6 to -2.2
Pixel size (Å)	0.729	0.729	0.729	0.729	0.729	0.729	0.729	0.729
Symmetry imposed	C1	C1	C1	C1	C1	C1	C1	C1
Initial particle images (no.)	640,335	640,335	537,060	537,060	564,777	564,777	371,973	371.973
Final particle images (no.)	115,543	115,543	136,652	136,652	155,321	155,321	52,547	52,547
Map resolution (Å)	2.9	3.2	2.8	3.2	3.0	3.4	3.3	3.8
FSC threshold	0.143	0.143	0.143	0.143	0.143	0.143	0.143	0.143
Map resolution range (Å)								
Refinement								
Initial model used								
Model resolution (Å)								
Model resolution range (Å)								
Map sharpening *B* factor (Å^2)	-55.41	-96.97	-48.71	-77.31	-60.25	-96.47	-64.62	-112.57
Model composition								
Non-hydrogen atoms	7957	6695	7837	5188	8051	6695	7909	4872
Protein residues	1043	847	1030	651	1058	847	1039	616
Ligands	0	1	0	1	0	1	0	0
B factors (Å^2)								
Protein	30.63	48.71	18.70	34.74	43.32	53.01	44.75	72.92
Ligand		43.83		27.33		37.25		
R.m.s. deviations								
Bond lengths (Å)	0.006	0.010	0.008	0.008	0.018	0.013	0.013	0.003
Bond angles (°)	0.827	1.105	0.856	1.116	1.096	0.873	1.047	0.668
Validation								
MolProbity score	2.01	2.1	2.03	2.9	2.19	2.21	2.25	1.82
Clashscore	11.34	12.50	13.46	21.80	13.77	16.79	17.37	11.64
Poor rotamers (%)	0	1.3	0.0	5.44	0	0.29	0	0
Ramachandran plot								
Favored (%)	93.30	94.47	94.17	91.29	90.25	92.03	91.37	96.39
Allowed (%)	6.7	5.16	5.73	8.71	9.55	7.97	8.53	3.61
Disallowed (%)	0.0	0.38	0.1	0.0	0.19	0.0	0.10	0.0

https://doi.org/10.1038/s41564-025-02168-4

Extended Data Table 2 | Potency of PTV and AMNV Against Resistant Variants

	HSV-1			HSV-2			VZV		
	Helicase[a]	Primase[b]	EC_{50} fold change	Helicase[a]	Primase[b]	EC_{50} fold change	Helicase[a]	Primase[b]	EC_{50} fold change
PTV	N342K		40[24]						
	G352V/R		400[26] / 3333[23]						
	M355T		>5[26], 15[59]						
	K356N/Q/T		>5000[20] / ≥100[22,26] / 100[23]	**K355N/T/R**		**210/50/10**			
	K356T	A899T	2500[23]	**K355R, L805I***	**A906V**	**1,300**			
		A899T	43[23]		**A906V**	**17**			
AMNV				N97T	S290N*	20[21]			
							N336K, R446H*	N939D*	~600[#25]
	G352C		**25**[21]	G351R		>2000[21]			
	G352V, M355I	S364G*	~650[58]						
	G352V, M355I	S364G*, R367H	~3000[58]						
	M355T		**6**[21]	M354I	S397G*	40[21]			
	K356N		**260**[21]	K355N/E/R		>2000/130/8[21]	**K350N**		**>2000**[57]
				K355T		**75**			
				K355N, K451R*		>1250[58]			
		F360V/C	**160/25**[21]						
		N902T	**9**[21]						

[a]HSV-1: UL5, HSV-2: UL-5, VZV: ORF55 [b]HSV-1: UL52, HSV-2: UL52, VZV: ORF6 *Substitutions unlikely to impact sensitivity to PTV or AMNV based on positioning in HP complex [#]Resistant culture reported to grow in 60 μM AMNV (EC_{50} = 0.1 μM) **Bold**, substitution(s) profiled in a recombinant virus.

https://doi.org/10.1038/s41564-025-02168-4

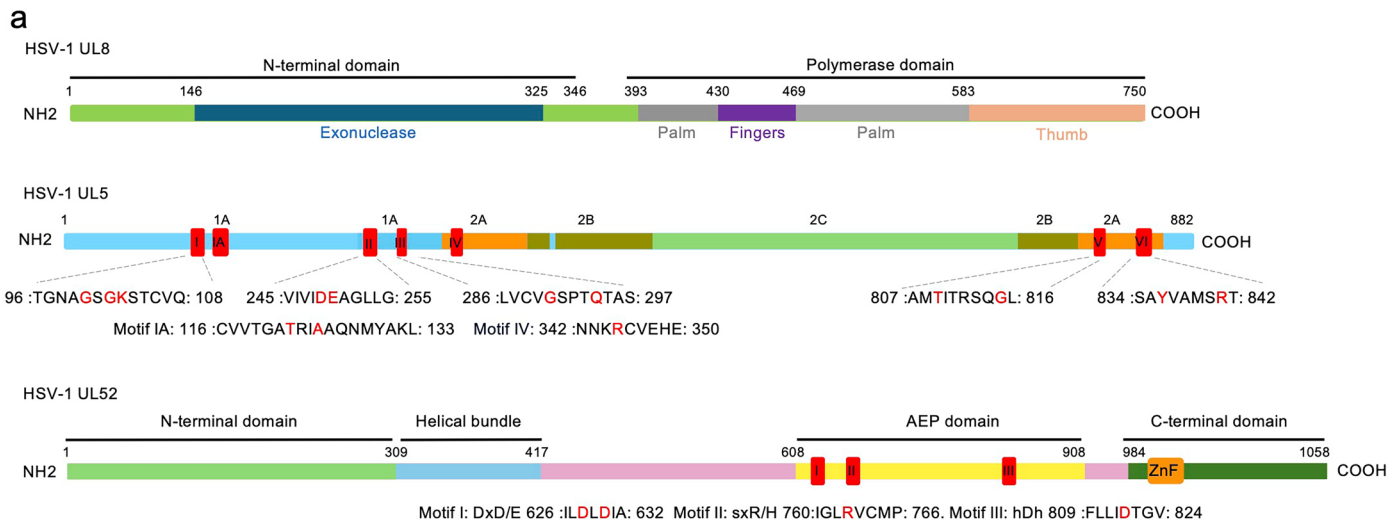

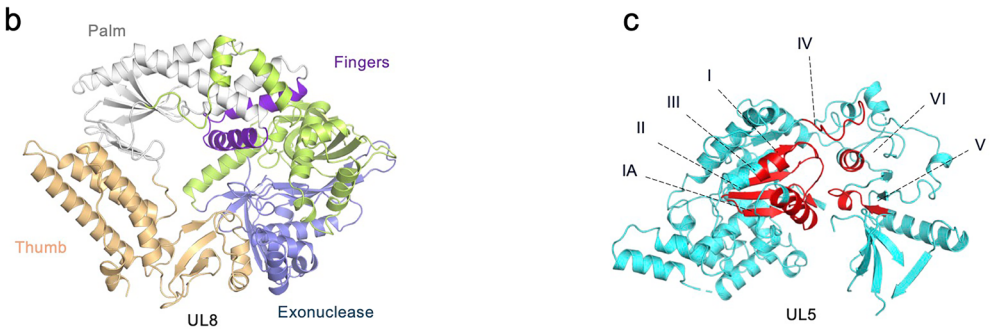

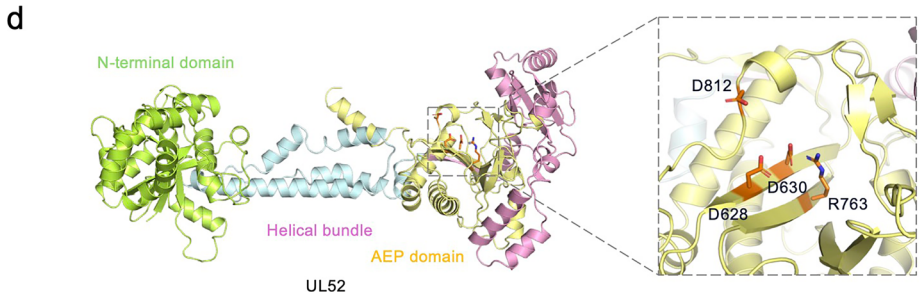

Extended Data Fig. 1 | Domain organization of the HSV-1 HP complex and structures of individual subunits. a, Linear representations of amino acid sequences illustrating the domain organization of the three subunits in HSV-1 HP complex: UL8 (with exonuclease, palm, fingers, and thumb subdomains), UL5 helicase (with seven motifs), and UL52 domains (N-terminal, AEP domain, three motifs, and zinc finger motif), adapted from Bermek and Williams[14]. The sequences of the three motifs in UL52 are shown below, with the catalytic residues highlighted in red. **b**–**d**, Ribbon diagrams of individual subunits in the solved structure of the HSV-1 HP complex with AMNV, using the same color scheme as in **a**. The seven motifs in UL5 and the three motifs in UL52 are highlighted in red, with catalytic residues in UL52 represented as orange sticks. The putative C-terminal domain and ZnF motif of UL52, depicted in (**a**), are not resolved and therefore are not shown in (**d**). The UL5 1B domain is not labeled in (**a**).

https://doi.org/10.1038/s41564-025-02168-4

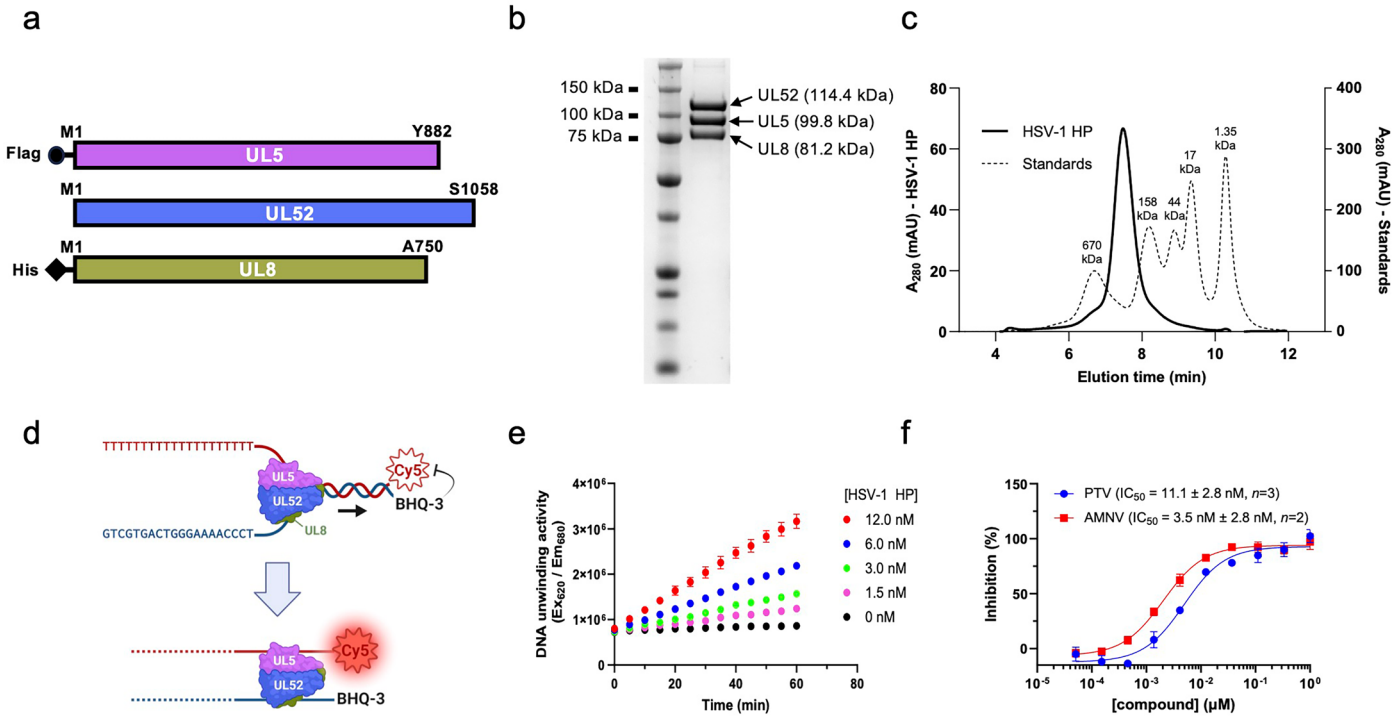

Extended Data Fig. 2 | Purification of HSV-1 HP complex. a, Constructs used for expression of HSV-1 HP subunits in insect cells. UL5 and UL8 were tagged N-terminally with Flag and His tags, respectively. **b**, Analysis of purity and integrity of UL5, UL52, UL8 subunits by SDS-PAGE and colloidal Coomassie stain. A representative image of two independent protein purification is shown. **c**, Analysis of the oligomeric status of the HP complex by SEC-HPLC using a Superose 6 Increase column. Elution profile of molecular weight standards shown with dotted line. mAU, milli-absorbance units. **d**, Schematic of the DNA unwinding assay. Unwinding of the forked DNA substrate releases the Cy5 fluorophore from the BHQ-3 quencher, allowing for emission of fluorescence. **e**, Evaluation of the helicase activity of the purified HSV-1 HP complex in the DNA unwinding assay depicted in panel **d**. Data are mean ± SD of measurements taken in triplicates. **f**, Inhibition of the HSV-1 HP complex by PTV (blue) and AMNV (red) in the DNA unwinding assay. Representative dose-response curves with a mean IC_{50} ± SD value from $n = 5$ independent experiments (PTV) and from $n = 2$ independent experiments (AMNV). Data points on graph are mean ± SD of 4 replicates per condition. Panel **d** created with BioRender.com.

https://doi.org/10.1038/s41564-025-02168-4

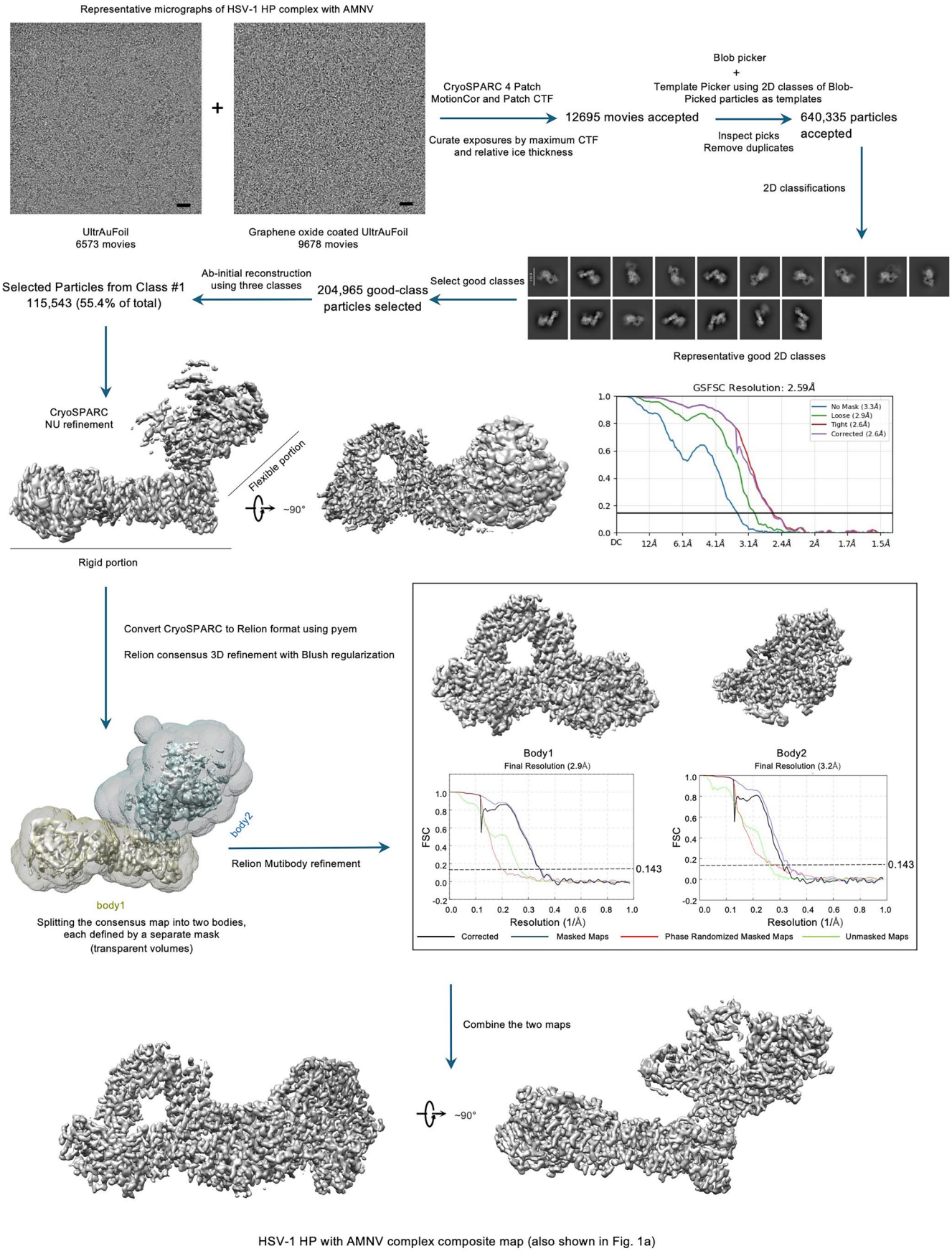

HSV-1 HP with AMNV complex composite map (also shown in Fig. 1a)

Extended Data Fig. 3 | See next page for caption.

https://doi.org/10.1038/s41564-025-02168-4

Extended Data Fig. 3 | Representative cryo-EM data processing scheme. Summary of the major steps of cryo-EM data processing for the HSV-1 HP complex with the AMNV dataset. The flowchart outlines each step in the process. Scale bars represent 20 Å in the micrographs and 130 Å in the 2D classification average. The gold-standard Fourier shell correlation (FSC) curve[54] shows an overall resolution of 2.6 Å at an FSC of 0.143, for the consensus map generated by CryoSPARC NU refinement. Transparent yellow and cyan surfaces represent the two masks used to separate the rigid and flexible bodies for Multibody refinement. FSC curves for each body's resolution, calculated in Relion Multibody refinement, are shown with designated lines. The final composite map used in Fig. 1a is also displayed.

https://doi.org/10.1038/s41564-025-02168-4

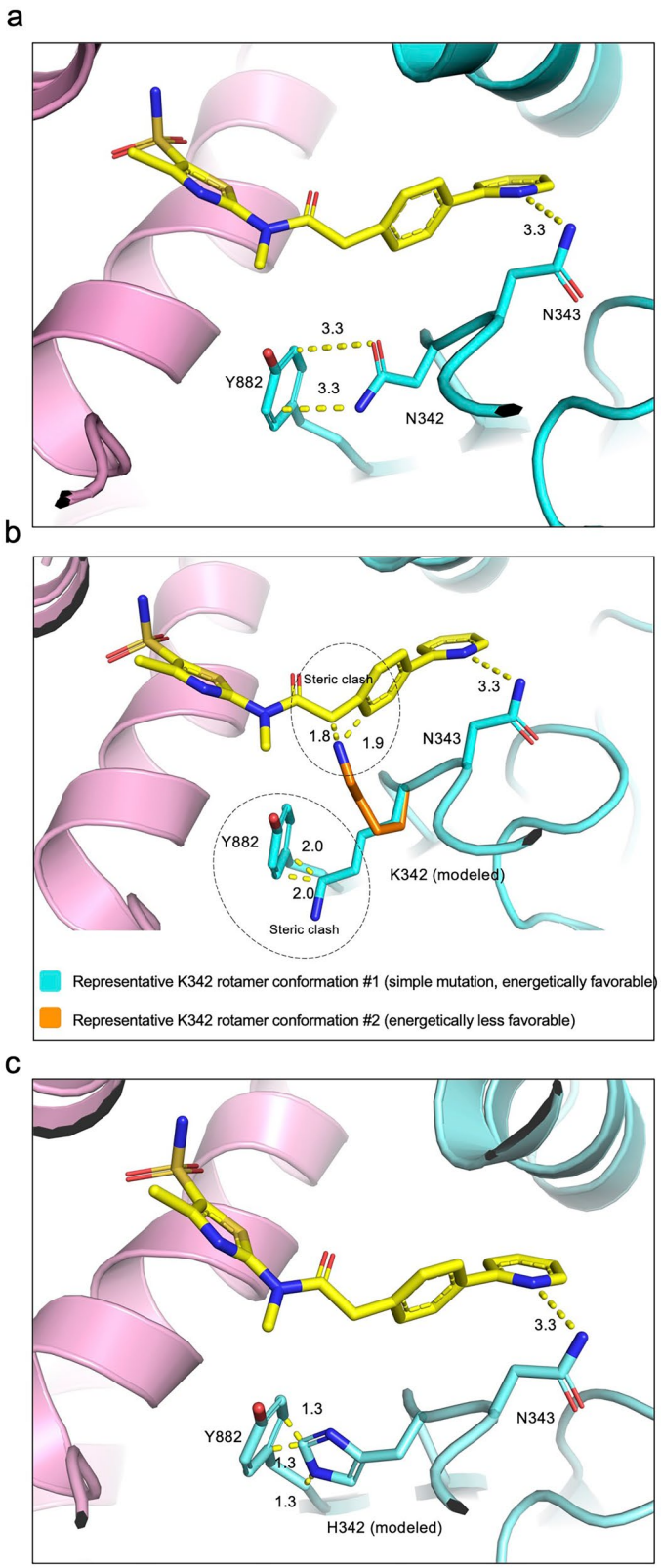

Extended Data Fig. 4 | Modeling of potential HSV-1 UL5 K342 and H342 rotamers. a, Cryo-EM structure of the HSV-1 HP complex with PTV at the binding site, showing PTV and UL5 residues N342, N343, and Y882 as stick representations. **b**, Same structure as in (**a**), showing two representative modeled conformations of K342: an energetically favorable conformation in cyan, and a less favorable conformation in orange. **c**, Same structure as in (**a**), showing the modeled conformation of H342 as sticks in cyan. Key distances between closely contacting atoms are represented as dashed lines, with measurements provided in Å.

https://doi.org/10.1038/s41564-025-02168-4

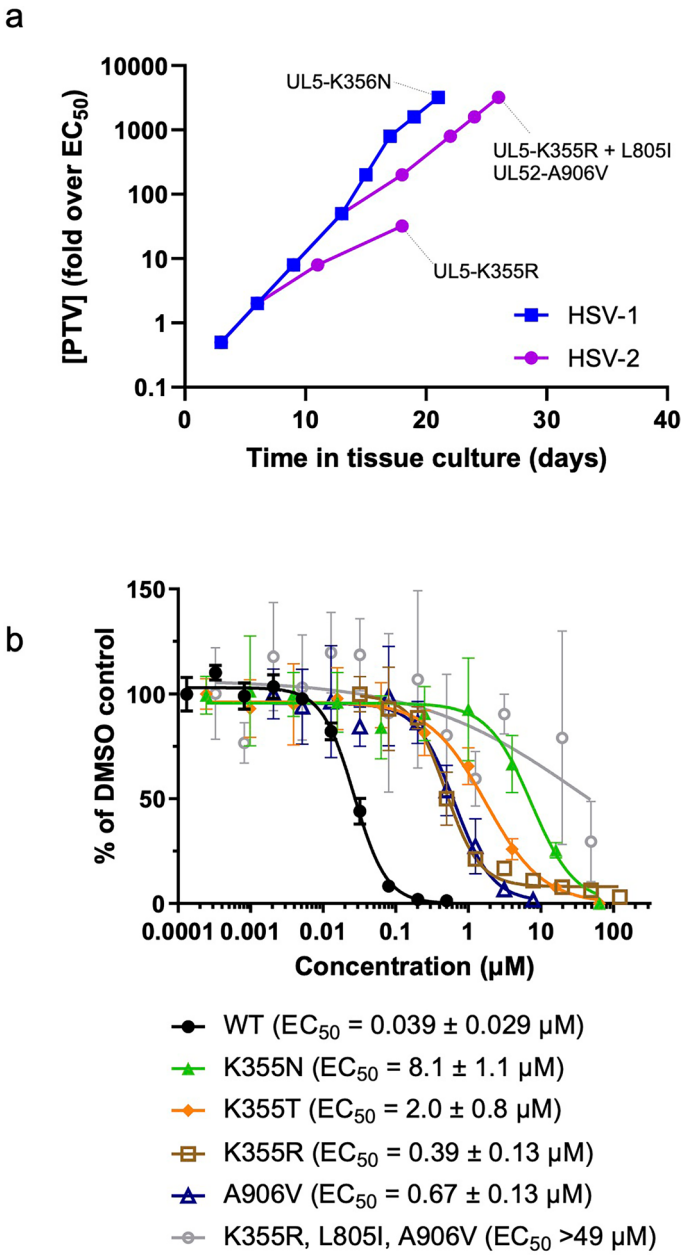

Extended Data Fig. 5 | Emergence of in vitro resistance in PTV dose-escalation studies. a, Cells infected with HSV-1 (blue) or HSV-2 (purple) were grown in the presence of PTV. When cytopathic effect was observed, virus from the culture supernatants was used to infect a fresh monolayer of cells in the presence of an increased concentration of PTV. Changes in HSV-1 and HSV-2 UL5/UL52 sequences compared to baseline (prior to PTV exposure) are indicated. DMSO-only passaged virus was used as a negative control for variant calling. **b**, Phenotyping of indicated HSV-2 variants was performed in ARPE-19 cells by measuring mCherry expression. Representative dose-response curves with a mean EC_{50} ± SD value from n = 3 independent experiments are shown. Data on graph are mean ± SD from 3-6 replicates per condition.

https://doi.org/10.1038/s41564-025-02168-4

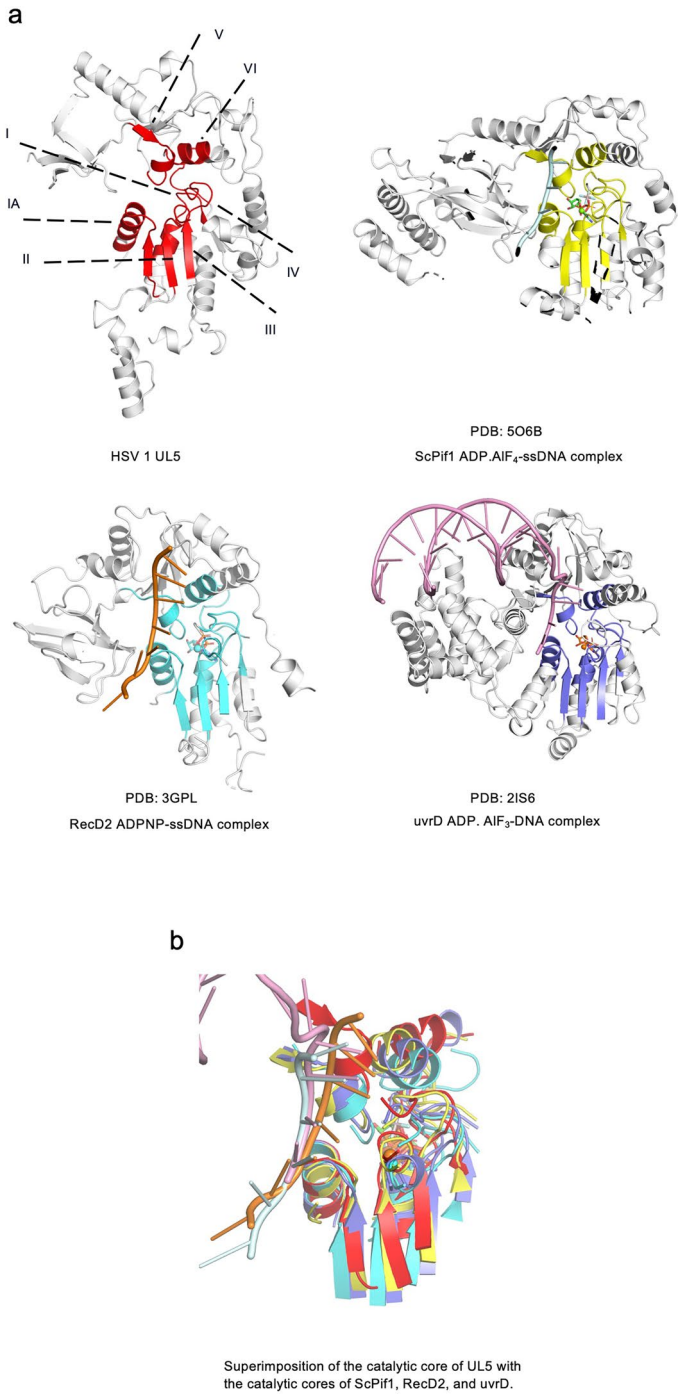

Extended Data Fig. 6 | HSV-1 UL5 shares a conserved catalytic fold with other SF1 family helicases. a, Structural comparison of UL5 with other SF1 helicases bound to ATP analogues and DNA substrates. Shown are UL5 (*upper left*), ScPif1 with ADP·AlF_4-ssDNA (*upper right*)[55], RecD2 with ADPNP and ssDNA (*lower left*)[27], and uvrD with ADP·AlF_3 and DNA (*lower right*)[56]. All structures are displayed as grey ribbon diagrams, with UL5's seven motifs highlighted in red. The corresponding seven motifs in other helicases are shown in distinct colors, and approximately aligned with UL5's seven motifs. ATP analogues are depicted as colored sticks, Mg^{2+} ions as spheres, and DNA backbones and individual bases as sticks in unique colors for clarity. **b**, Comparison of the active sites of UL5 and other helicases depicted in (**a**). The superimposition is based on the seven conserved motifs of UL5 and equivalent motifs in other SF1 helicases, with consistent color scheme and style as in (**a**).

https://doi.org/10.1038/s41564-025-02168-4

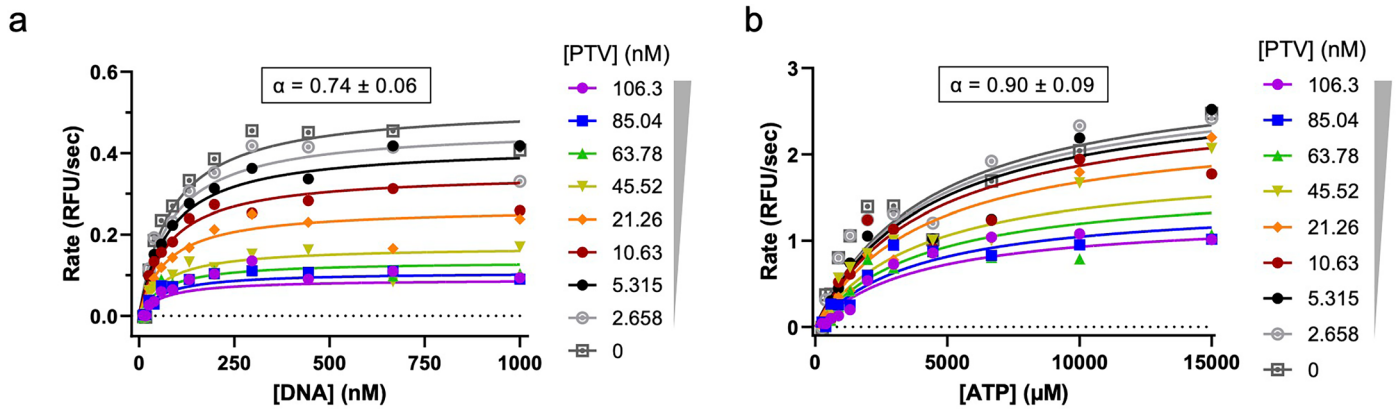

Extended Data Fig. 7 | Mechanism of action assay for HSV-1 HP. Substrate competitiveness of PTV against DNA (**a**) and ATP (**b**) was measured at various concentrations of inhibitor. Results from a representative experiment are shown. α-factors were calculated from the global fit of the data using a mixed inhibition model and are displayed as mean values ± SD of two independent replicates (α > 1 is competitive, α ≈ 1 is non-competitive, α < 1 is uncompetitive).

https://doi.org/10.1038/s41564-025-02168-4

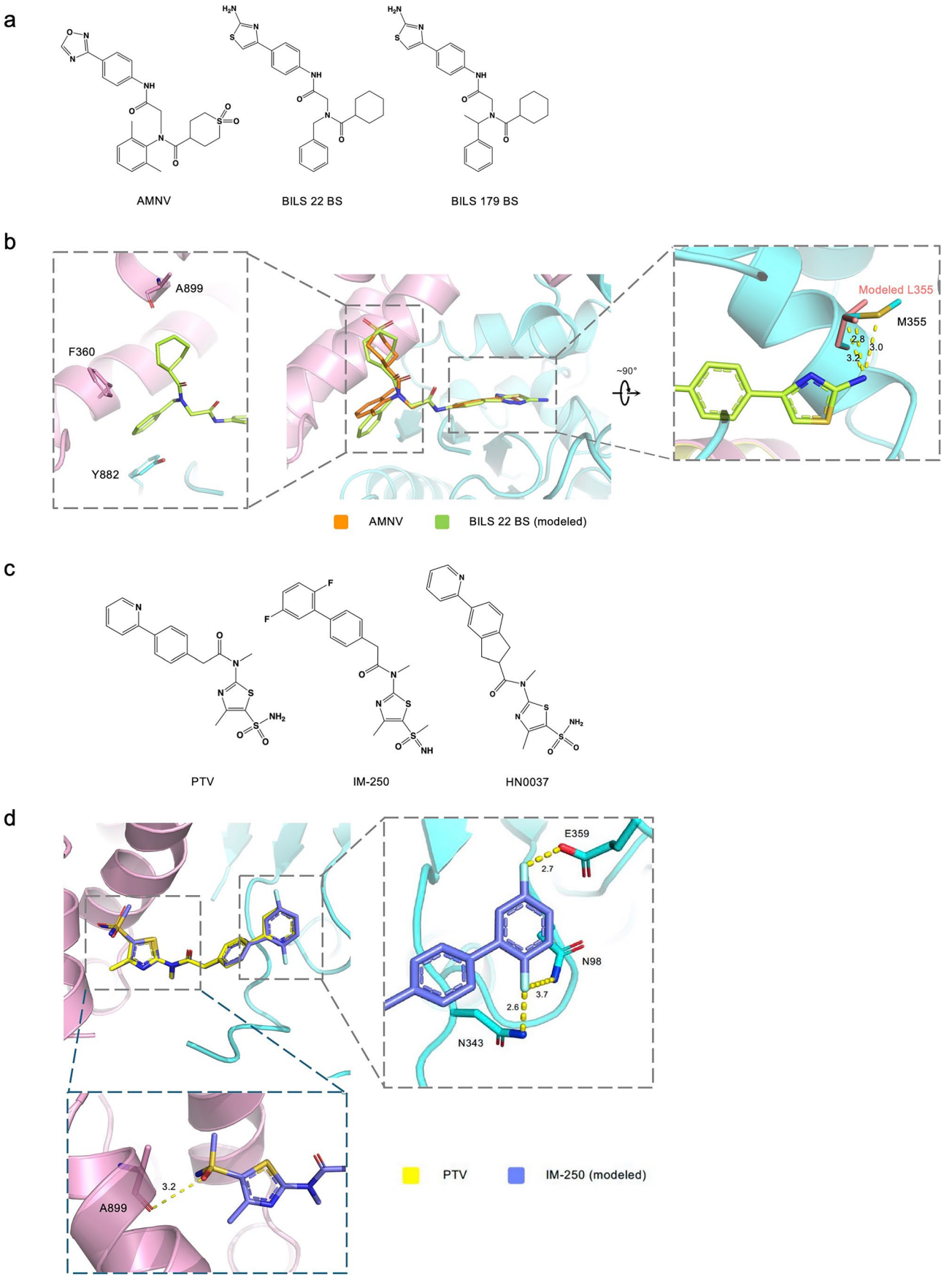

Extended Data Fig. 8 | See next page for caption.

https://doi.org/10.1038/s41564-025-02168-4

Extended Data Fig. 8 | Structural comparison of HPI series and modeling of BILS 22 BS binding to HSV-1 HP. a, Chemical structures of AMNV (*left*), BILS 22 BS (*middle*), and BILS 179 BS (*right*), positioned in a similar orientation. **b**, Modeling of BILS 22 BS and UL5 L355 based on the AMNV structure and UL5 M355 as templates. The color scheme is indicated and distances between closely contacting atoms are represented as yellow dashed lines with measurements provided in Å. **c**, Chemical structures of PTV (*left*), IM-250 (*middle*), and HN0037 (*right*), positioned in a similar orientation. **d**, Modeling of IM-250 using the PTV structure as a template. The closely contacting atoms are represented following the color scheme described in (**b**).

nature portfolio

Corresponding author(s): Qing Yao, Alexandre Mercier

Last updated by author(s): Aug 12, 2025

Reporting Summary

Nature Portfolio wishes to improve the reproducibility of the work that we publish. This form provides structure for consistency and transparency in reporting. For further information on Nature Portfolio policies, see our Editorial Policies and the Editorial Policy Checklist.

Statistics

For all statistical analyses, confirm that the following items are present in the figure legend, table legend, main text, or Methods section.

n/a	Confirmed	
☐	☒	The exact sample size (*n*) for each experimental group/condition, given as a discrete number and unit of measurement
☐	☒	A statement on whether measurements were taken from distinct samples or whether the same sample was measured repeatedly
☒	☐	The statistical test(s) used AND whether they are one- or two-sided *Only common tests should be described solely by name; describe more complex techniques in the Methods section.*
☒	☐	A description of all covariates tested
☒	☐	A description of any assumptions or corrections, such as tests of normality and adjustment for multiple comparisons
☐	☒	A full description of the statistical parameters including central tendency (e.g. means) or other basic estimates (e.g. regression coefficient) AND variation (e.g. standard deviation) or associated estimates of uncertainty (e.g. confidence intervals)
☒	☐	For null hypothesis testing, the test statistic (e.g. *F*, *t*, *r*) with confidence intervals, effect sizes, degrees of freedom and *P* value noted *Give P values as exact values whenever suitable.*
☒	☐	For Bayesian analysis, information on the choice of priors and Markov chain Monte Carlo settings
☒	☐	For hierarchical and complex designs, identification of the appropriate level for tests and full reporting of outcomes
☒	☐	Estimates of effect sizes (e.g. Cohen's *d*, Pearson's *r*), indicating how they were calculated

Our web collection on statistics for biologists contains articles on many of the points above.

Software and code

Policy information about availability of computer code

Data collection	ThermoFisher EPU 3.5
Data analysis	GraphPad Prism 10.2.3, Microsoft® Excel® for Microsoft 365 MSO (Version 2402 Build 16.0.17328.20550) 64-bit, CryoSPARC-v.4.6.0, Relion5.0, Coot 0.9.8.7, Chimera 1.16, Phenix 1.19.1, PyMOL 2.5.2, T coffee server, GeneDoc 2.7

For manuscripts utilizing custom algorithms or software that are central to the research but not yet described in published literature, software must be made available to editors and reviewers. We strongly encourage code deposition in a community repository (e.g. GitHub). See the Nature Portfolio guidelines for submitting code & software for further information.

Data

Policy information about availability of data

All manuscripts must include a data availability statement. This statement should provide the following information, where applicable:

- Accession codes, unique identifiers, or web links for publicly available datasets
- A description of any restrictions on data availability
- For clinical datasets or third party data, please ensure that the statement adheres to our policy

The cryo-EM density maps generated in this study have been deposited in the Electron Microscopy Data Bank under the following accession codes: EMDB-49269, EMDB-49326; EMDB-49304, EMDB-49306; EMDB-49290, EMDB-49291; EMDB-49276 and EMDB-49277. Each pair corresponds to the two bodies of the HSV-1 HP complex with AMNV, the HSV-1 HP complex with PTV, the HSV-1 HP complex prepared with DNA, ATP-γ-S, Mg^{2+}, and PTV, and the HSV-1 HP complex prepared with

DNA, ATP-γ-S, and Mg^{2+}, respectively. The corresponding atomic coordinates for the structural models have been deposited in the Protein Data Bank under the following accession codes: 9NDA, 9NEL; 9NEB, 9NEE; 9NDZ, 9NE0; 9NDQ and 9NDT, with each pair representing the two bodies of the respective complex. All other relevant data generated and analyzed during this study are included in this article and its supplementary information. Should any raw data files be needed in another format they are available from the corresponding author upon reasonable request. All other relevant data generated and analyzed during this study are included in this article and its supplementary information. Should any raw data files be needed in another format they are available from the corresponding author upon reasonable request.

Research involving human participants, their data, or biological material

Policy information about studies with human participants or human data. See also policy information about sex, gender (identity/presentation), and sexual orientation and race, ethnicity and racism.

Reporting on sex and gender	N/A
Reporting on race, ethnicity, or other socially relevant groupings	N/A
Population characteristics	N/A
Recruitment	N/A
Ethics oversight	N/A

Note that full information on the approval of the study protocol must also be provided in the manuscript.

Field-specific reporting

Please select the one below that is the best fit for your research. If you are not sure, read the appropriate sections before making your selection.

☒ Life sciences ☐ Behavioural & social sciences ☐ Ecological, evolutionary & environmental sciences

For a reference copy of the document with all sections, see nature.com/documents/nr reporting summary flat.pdf

Life sciences study design

All studies must disclose on these points even when the disclosure is negative.

Sample size	No statistical methods were used to predetermine sample size. Biochemical and cell-based assays were performed with at least 2 independent experiments and had excellent reproducibility; mean +/- standard deviation was used for statistical analysis as commonly used for these techniques.
Data exclusions	Data from all virology and biochemical independent experiments were included. For cryo-EM analyses, particles that did not contribute to improving map quality were excluded according to the standard classification procedures in cryoSPARC and Relion.
Replication	All biochemical and functional assays were independently repeated at least twice, the majority 3-5 times. Data reproducibility was excellent.
Randomization	For cryo-EM analyses, particles were randomly assigned to half-maps for resolution determination, following standard procedures in cryoSPARC and Relion. For biochemical analysis, randomization was not relevant to this study.
Blinding	Blinding was not relevant to this study since neither structural nor functional experiments included subjective assignments.

Reporting for specific materials, systems and methods

We require information from authors about some types of materials, experimental systems and methods used in many studies. Here, indicate whether each material, system or method listed is relevant to your study. If you are not sure if a list item applies to your research, read the appropriate section before selecting a response.

Materials & experimental systems

n/a	Involved in the study
☒	☐ Antibodies
☐	☒ Eukaryotic cell lines
☒	☐ Palaeontology and archaeology
☒	☐ Animals and other organisms
☒	☐ Clinical data
☒	☐ Dual use research of concern
☒	☐ Plants

Methods

n/a	Involved in the study
☒	☐ ChIP-seq
☒	☐ Flow cytometry
☒	☐ MRI-based neuroimaging

Eukaryotic cell lines

Policy information about cell lines and Sex and Gender in Research

Cell line source(s)	Vero and ARPE-19 cell lines were purchased from ATCC.
Authentication	Vero and ARPE--19 cell lines were not authenticated as they were purchased commercially.
Mycoplasma contamination	Vero and ARPE--19 cell lines were not tested for mycoplasma contamination.
Commonly misidentified lines (See ICLAC register)	None.

Plants

Seed stocks	*Report on the source of all seed stocks or other plant material used. If applicable, state the seed stock centre and catalogue number. If plant specimens were collected from the field, describe the collection location, date and sampling procedures.*
Novel plant genotypes	*Describe the methods by which all novel plant genotypes were produced. This includes those generated by transgenic approaches, gene editing, chemical/radiation-based mutagenesis and hybridization. For transgenic lines, describe the transformation method, the number of independent lines analyzed and the generation upon which experiments were performed. For gene-edited lines, describe the editor used, the endogenous sequence targeted for editing, the targeting guide RNA sequence (if applicable) and how the editor was applied.*
Authentication	*Describe any authentication procedures for each seed stock used or novel genotype generated. Describe any experiments used to assess the effect of a mutation and, where applicable, how potential secondary effects (e.g. second site T-DNA insertions, mosiacism, off-target gene editing) were examined.*